A REVIEW OF AERONAUTICAL FATIGUE AND STRUCTURAL INTEGRITY IN ISRAEL
(2015 –2016)

Compiled by:
Dr. Yuval Freed
Engineering Division
Israel Aerospace Industries
***Ben-Gurion Airport,* Israel**
yfreed@iai.co.il

Presented at the 35th Conference of the International Committee on Aeronautical Fatigue and Structural Integrity (ICAF)
Nagoya, Japan
5-6 June 2017

A REVIEW OF AERONAUTICAL FATIGUE AND STRUCTURAL INTEGRITY IN ISRAEL

JANUARY 2015 – DECEMBER 2016

SUMMARY

This review summarizes fatigue, structural-integrity and fracture-mechanics investigations that were performed in Israel during the period of April 2015 to March 2017. The review includes contributions from Israel Aerospace Industries Ltd. (IAI), Israel Air Force (IAF), Tel-Aviv University (TAU), Ben-Gurion University (BGU), Technion and Weizmann Institute.

Presented at the 35th ICAF Conference
Nagoya, Japan
5-6 June 2017

TABLE OF CONTENTS

A REVIEW OF AERONAUTICAL FATIGUE INVESTIGATIONS IN ISRAEL APRIL 2015 – MARCH 2017

1. INTRODUCTION

The Israel National Review summarizes activities performed in the field of aeronautical fatigue, structural integrity, health monitoring and fracture mechanics in Israel during the period of January 2015 to December 2016. The previous National Review [1] covered activities up to the beginning of 2015. The following organizations contributed to this review:

- Israel Aerospace Industries Ltd. (IAI)
- Israel Air Force (IAF)
- Tel-Aviv University (TAU)
- Ben-Gurion University (BGU)
- Technion
- Weizmann Institute

The National Review was compiled by Dr. Yuval Freed (yfreed@iai.co.il).

2. FATIGUE ANALYSIS, TESTING AND LIFE EXTENSION

2.1 A Summary of New IAI Executive Jet Full Scale Fatigue Test (Y. Buimovich, Y. Freed, G. Noivirt, C. Matias, IAI)

Israel Aerospace Industries and another aerospace company have jointly developed a new super mid-size executive jet. The aircraft has a range of 3,400 nautical miles at a maximum speed of Mach 0.85. It can cruise at altitudes up to 45,000 feet. Its first flight took place during December 2009. Certification to the FAA, EASA, CAAI and TCCA regulations were completed, and type-certificates were obtained. Deliveries began in 2012.

The aircraft is powered by twin Honeywell HTF7250G engines, each producing 7,445 pounds of thrust. The aircraft is capable of nonstop flight from New York to London or from London to Dubai. The aircraft has a very roomy and quiet cabin. The cabin environment includes 100% fresh air and a cabin altitude not exceeding 7,000 feet. Its Design Life Goal (DLG) is 20,000 flights or 36,000 flight-hours.

As part of its damage-tolerance certification program, a structurally complete airframe test-article was fatigue tested for two lifetimes (40,000 flights), followed by half a lifetime (10,000 flights) of damage-tolerance testing with artificial flaws inflicted at selected critical locations. Residual strength tests, under limit loads and cabin pressurization, were performed in the presence of large cracks at several critical locations. It should me mentioned that some of these large cracks were "naturally" developed and allowed to grow, and the other were artificially implemented. The last test phase will be teardown inspection for selected areas.

The test article consisted of a structurally complete airframe representing of serial production, including the entire empennage structure, dummy leading gears and engines with their serial production structure attachments. The vertical stabilizer, horizontal stabilizer, elevators, scissors, pivot fitting and dummy horizontal stabilizer trim actuator (HSTA) were also included in the fatigue test-article. Figure 1 shows the fatigue test-article mounted in its loading fixture upon completion of two and a half lifetimes (50,000 flights). Figure 2 presents a schematic view of the fatigue test setup, and showing the loading system. The landing gears, rudder, flaps, spoilers and ailerons were substantiated by fatigue testing in the component level.

The full-scale fatigue test loading spectrum included a complete set of symmetric and asymmetric fatigue flight loads spectra, including engine thrust reverser buffeting loading on the empennage and a suitable representation of engine support loading and main landing gear backup structure ground loading spectra. The loading spectrum contained 57 cycles per flight (approximately 10-12 minutes per flight). Loads were applied through 58 loading zones and were reacted at six locations. A cabin pressure differential of 9.2 psi was applied during each flight. Periodic inspections for cracks were performed at planned periodical intervals using various NDI methods (as prescribed by the Damage Tolerance justification analyses). Periodically, a total of more than 1,500 strain-gauge measurements were recorded, under a set of calibration loads, in order to determine if any significant fatigue damage had occurred at

various critical locations. The full scale fatigue test was launched on March, 2011, and completed two lifetimes by March, 2014.

Figure 1. Complete Airframe Mounted in its Fixture upon completion of two and a half lifetimes (50,000 flights)

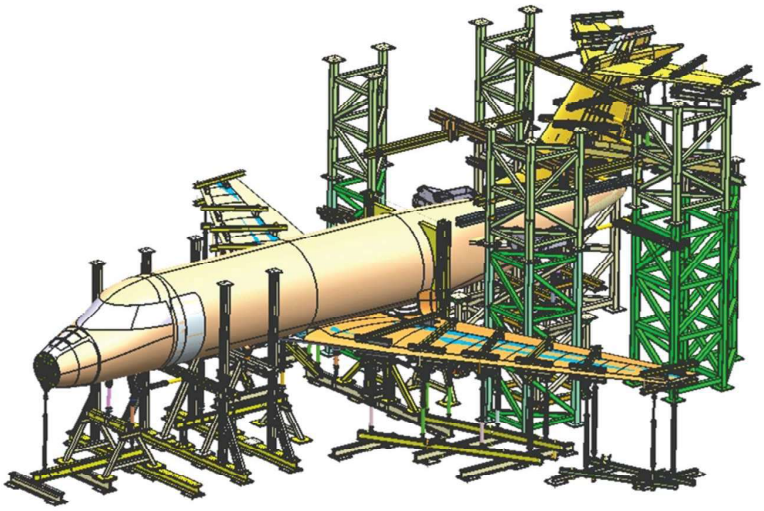

Figure 2. Schematic View of the Fatigue Test Setup

Total of 42 different crack findings were reported in scheduled inspections during the two lifetimes cyclic testing. These findings were scattered within 23 structural elements in the aircraft. Most of these findings did not require structural repair/modification, but the cracks were permitted to continue growing under monitoring of their growth. Other findings (at two elements) did require relevant design improvements and retrofits were employed in fleet to ensure the structural integrity of the aircraft. The aircraft maintenance manual was updated accordingly. It should be mentioned that all the crack findings that were left to grow and

monitored presented steady crack growth rates that positively validated the planned scheduler inspection program to fleet.

At the end of two lifetimes (40,000 flights) of cyclic testing, 17 artificial flaws were introduced at several critical locations. An example of implementation of artificial crack in the RHS wing front spar web is shown in
Figure 3. Impact damages conducted on the horizontal tail composite skin are shown in Figure 4. The damage-tolerance test phase was scheduled for another half a lifetime (10,000 flights), in order to ensure that sufficient crack growth data will be collected. In addition to the artificial flaws, certain cracks detected during fatigue testing were not repaired and their crack growth rates were closely monitored during the damage-tolerance testing. Crack growth gauges were installed at crack tips to monitor the growing cracks until the end of the damage-tolerance phase of this test. The damage tolerance phase started on May, 2014, and completed half lifetime (10,000 flights) by June, 2015.

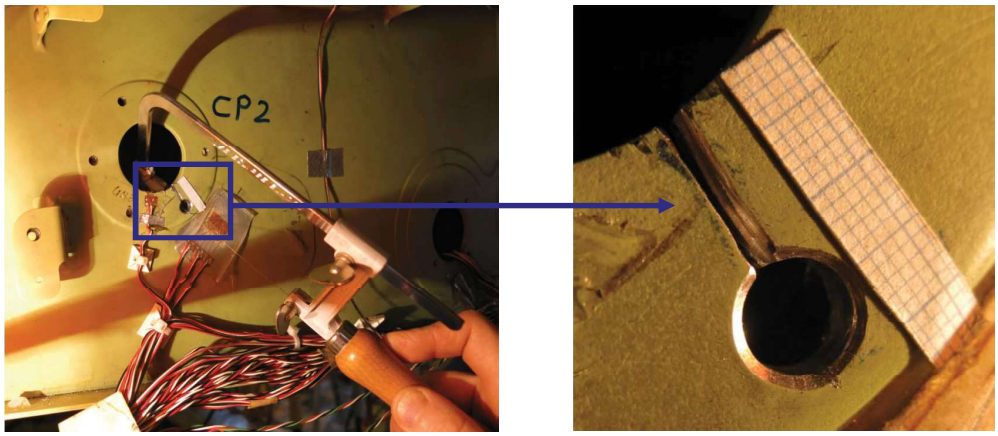

Figure 3. An example of artificial crack at the wing front spar web penetrations-RHS

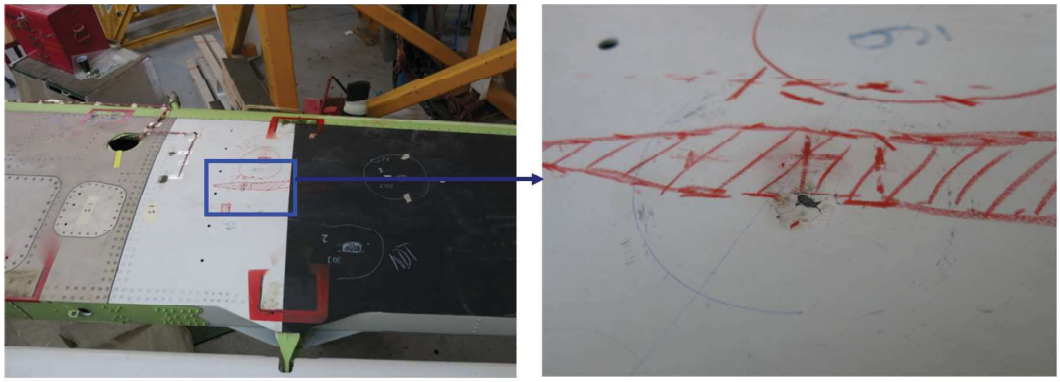

Figure 4. Impact damage conducted on the horizontal tail composite skin

Total of 24 different new findings were reported in scheduled inspections during the half lifetime cyclic of the damage tolerance test. These findings were scattered within 20 structural elements in the aircraft. Most of these cracks were not repaired and monitored until the end of the test, since they were detected after two lifetimes. However, three cracked elements were repaired to avoid possible multi element damage scenario and to ensure the structural integrity of the aircraft for the rest of the test and at the residual strength phase.

The 66 crack findings that were reported in scheduled inspections during the two and a half lifetimes of cyclic testing were scattered within 43 structural elements in the aircraft. Figure 5, Figure 6 and Figure 7 illustrate that structural elements in which the cracks were scattered in. At the fuselage, the cracks are concentrated at the cockpit, main entrance door, emergency door and baggage door. At the empennage, several cracks were reported at the vertical tail to fuselage attachment. At the wing the cracks were detected at the front spar and at several inboard ribs.

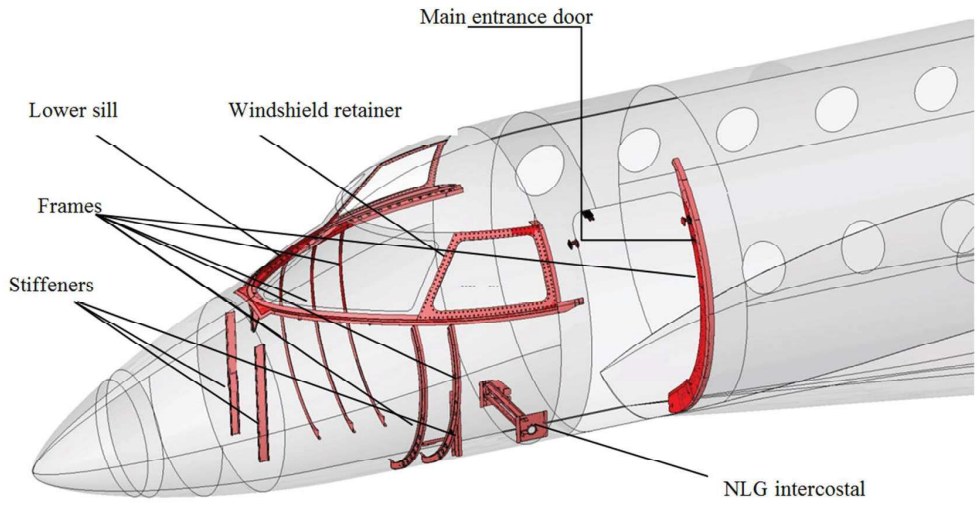

Figure 5. Cracked elements at the cockpit and Fwd fuselage

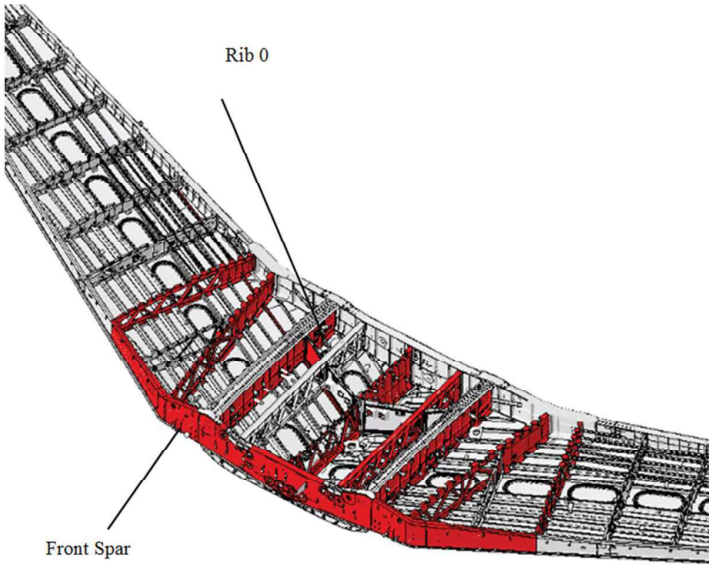

Figure 6. Cracked elements at the wings

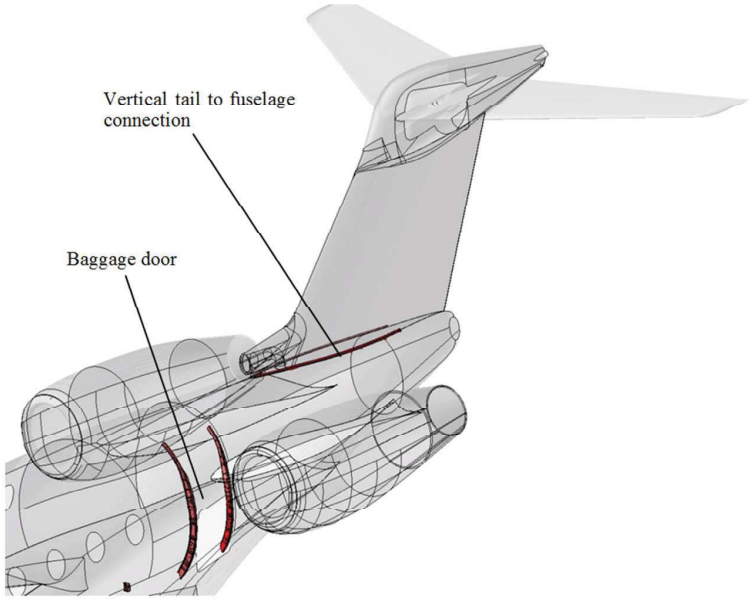

Figure 7. Cracked elements at the Baggage door surrounding and empennage

At the end of the cycling tests, residual strength tests were performed for certain load cases, as required by FAR 25.571(b) regulations. In this test, a two-bay crack in the fuselage was implemented, to demonstrate that the structure can withstand large discrete source damages. Figure 8 presents the wing residual strength test in the presence of a two bay crack inflicted in its wing.

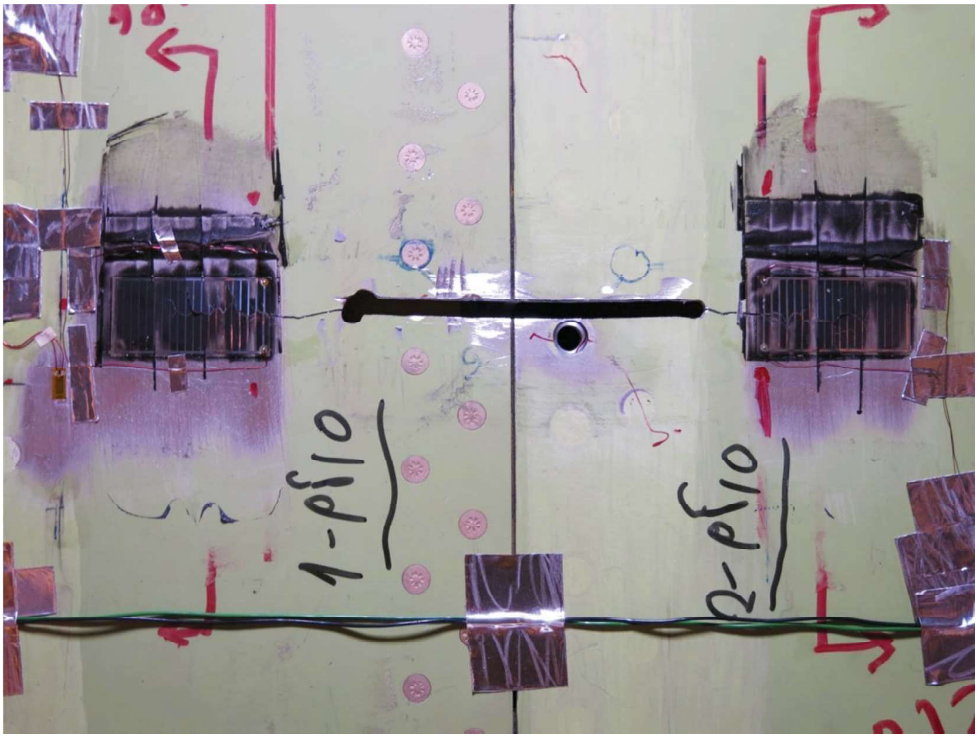

Figure 8. Large crack (with broken stringer) at the wing tested in the Residual Strength test

To summarize, the test results of two and a half lifetimes presented the following achievements:

- A reasonable amount of total crack findings for such scale of fatigue testing. I.e., a much larger amount of findings could imply of "under" structural design (poor design), and much lower amount of findings, could imply of "over" structural design. The presented findings imply that the structure is well designed and is structural damage tolerant.
- The test sequence addressed relatively well the planned schedule of the test. Obviously, for such scale of tests, this may not be taken for granted.

More details on the test preparations, test setup and test results are provided in Ref. 2.

2.2 IAI Executive jet main landing gear fatigue test (Y. Freed, IAI)

As part of IAI newly executive jet certification process, the Main Landing Gear (MLG) was fatigue tested for five lifetimes (20,000 flights × 5 = 100,000 flights) to demonstrate compliance with safe-life requirements of FAR §25.571(c). Prior to this test, several other certification tests were conducted, such as drop test (comply with FAR §25.473 and §25.723) and a static test up to ultimate load.

The drop test carriage was loaded to the test specimen with the appropriate weight, so that the total carriage mass, including test adaptors, was set to the requirements. In order to comply with regulations, the drop test was started at a vertical speed of 1.0 m/sec, and was gradually increased in steps of 0.5 m/sec up to 3.66 m/sec. The impact platform in this test was built as a light but rigid construction, equipped with 6 load cells for measuring vertical, longitudinal and side loads during impact. The platform was cleaned of rubber deposits between drops, so it maintained similar surface condition for each test. The surface roughness of the impact platform was chosen carefully to represent the expected coefficient of friction.

The static test consisted of ten different loading cases, six of them are for the extended position and four for the retracted position. During testing, strain were measured by means of strain gauges and compared to finite element model predictions. Test results demonstrated that the MLG can withstand its design ultimate loads without any failure.

The MLG fatigue test consisted of the landing gear entire ground loads spectrum that includes taxiing, braking, engine run-up, turning, pivoting, take-off and landing impact. The fatigue test consisted of five blocks, each representing full lifetime of the gear (20,000 landings). Each block was divided into two segments, each representing 10,000 landings. At each segment the landing gear was loaded in its extended position, and then in its retracted position. Illustrations of the extended and retracted positions are shown in Figure 9. In its retracted position the side brace was subjected to 12,000 simulated flights per segment, simulating in-flight loading of the gear as well as additional 20% cycles applying during maintenance actions of the landing gear. The total number of simulated flights in the test represents a scatter factor of 5 (100,000 flight cycles are applied in test). A picture of the landing gear mounted in its test rig is shown in Figure 10.

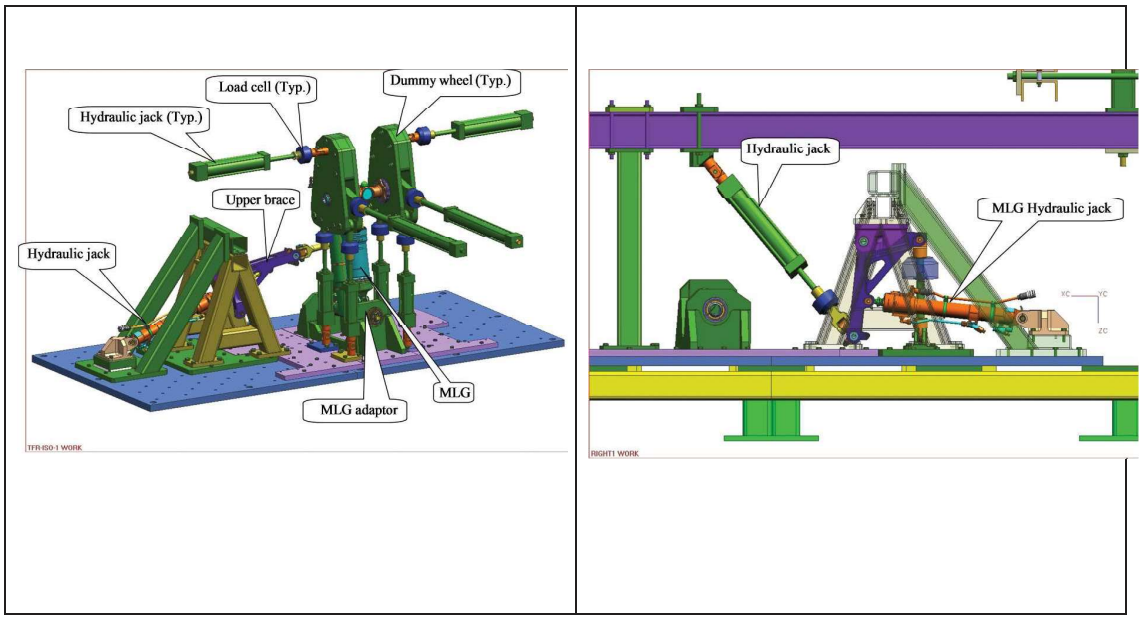

Figure 9. The MLG in its Extended (left) and Retracted (right) Configurations

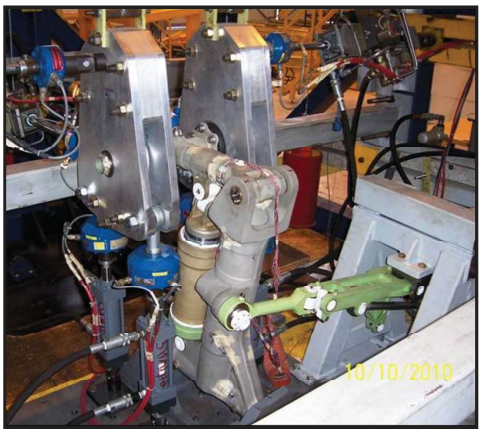

Figure 10. Main Landing Gear Fatigue Testing

The MLG fatigue test was completed successful on October 2015. Any findings reported during test were addressed by design improvements and implemented in fleet as well as in serial productions.

2.3 IAI Executive Jet, Flap Fatigue Test (C. Matias, IAI)

As part of IAI new executive jet damage-tolerance certification program, the wing flap was fatigue tested for two lifetimes followed by half a lifetime damage tolerance phase with presence of additional artificial damages (for total of 50,000 simulated flights). These testing phases were followed by residual strength testing with presence of a large crack at critical locations. The test was conducted at the National Institute for Aviation Research (NIAR) Full Scale Structural Test Laboratory located in Wichita, KS.

The test article is a full scale production flap assembly. The article was mounted on a test fixture representing the rear spar of the wing box. Aerodynamic loads were applied by load pads and patches bonded to the surface of the flap and loaded by a whiffletree load distribution apparatus. A single wing bending case was applied throughout the duration of the fatigue and damage tolerance portion of the test. A separate wing bending case was applied for the residual strength test. The flap was instrumented with strain gages. Strain gage data surveys were taken at the beginning of the test and periodically throughout the test in order to monitor the structural integrity of the test article. Additionally, the strain gages data provided information on load distribution and for correlation to the finite element model used for the analyses. Picture of the test article mounted in its test rig is shown in Figure 11.

The test was composed of three stages. First, fatigue test was conducted to two lifetimes, representing 40,000 simulated flights. Next, damage tolerance Test (½ lifetime), including infliction of discrete damage to the flap in key fatigue sensitive areas. Finally, residual strength test, by applying the flap design limit load with the presence of crack lengths of

“near” the crack growth stability critical crack length to demonstrate residual strength in accordance with FAR 25.571. These “near” critical length cracks were achieved by spontaneous "natural" crack growth. In addition, the test includes compliance to FAR 25.671 for presentation of single element failure. Completion of test is followed by teardown detailed inspections.

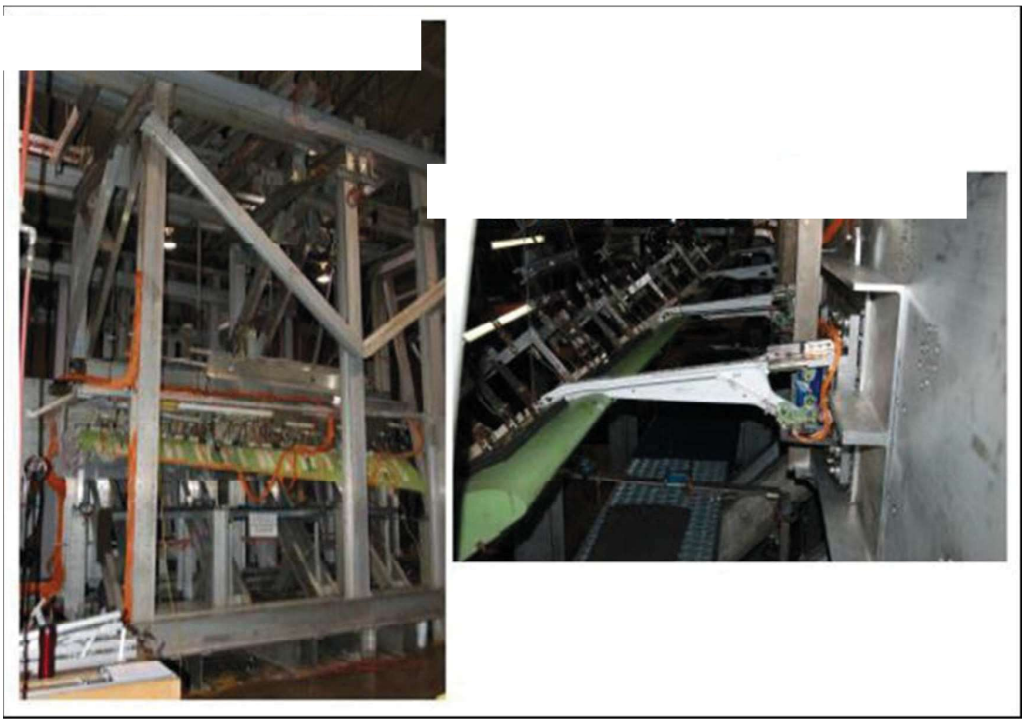

Figure 11. Flap test setup and the loading system

Few cracks were detected at some of the flap tracks roller fittings, Ribs, Skin cutouts and Actuator fitting. All these findings were fully analyzed and design changes were introduced to these items and incorporated into the fleet.

2.4 IAI New Special Mission Aircraft (E. Cohen, Y. Freed, IAI)

Israel Aerospace Industries and Bombardier Aerospace have jointly developed a new special mission aircraft based on Bombardier G5000 large business jet platform. The special mission includes installation of a pod at the aircraft belly, Satellite Communication (SATCOM) antenna on its crown, ventral fins, vertical tail bullet, Line of Sight (LOS) antenna and additional communication antennas installed in different locations at the fuselage.

The program was initiated on July 2011. The first aircraft arrived to IAI facilities on June 2012. First flight took place on December 2013, and a supplemental Type Certificate (STC) was awarded to IAI by the Israeli civil aviation authority (CAAI) by the end of 2014, after completion of approximately 50 test flights. The last modified aircraft was delivered to the

customer on 2015. Figure 1 presents the special mission aircraft configuration with its installations.

Figure 12. IAI new special mission aircraft

During the development of this platform, IAI has faced several engineering challenges, such as minimizing the changes to the green aircraft and its systems, all by maintaining commonality to the standard G5000 fleet. Since the mission profile of this aircraft is different than that of the G5000 business jet, a full aircraft assessment was obtained and the green aircraft inspection program was adjusted accordingly. The special mission installations required design of a new backup structure, including replacements and reinforcements of fuselage frames, installation of skin doublers, and reinforcement of the Aft fuselage structure f or the installation of ventral fins. These modifications are illustrated in Figure 13.

Figure 13. Installations and reinforcements involved in IAI new special mission aircraft

2.5 FMA IA-58H Pucara engine upgrade structural substantiation program (Y. Freed, IAI)

Israel Aerospace Industries has recently completed the design, manufacture and assembly of an upgraded engine for the Fabrica Argentina de Aviones (FAdeA) Pucara light strike aircraft, also referred to as IA-58H.

The engine upgrade program included installation of Pratt & Whitney PT-6A-62 engines with four-bladed propellers in place of the original incumbent Turbomeca Astazou XVIG units with three-bladed propellers. Another enhancement for the IA-58H is the integration of modern avionics for compatibility with the FAdeA IA-63 Pampa advanced jet trainer and light attack jet. This new avionics suite includes a multifunctional display screen in each cockpit, hand-on-throttle-and-stick controls, cockpit and engine armour, modern communications systems, and the replacement of obsolete parts. The upgraded aircraft is shown in Figure 9. The upgraded Pucara aircraft took its first flight on November, 2015.

Figure 14. FMA IA-58H Pucara with upgraded engines installed

As part of the engine installation substantiation full scale static and fatigue tests were conducted to the welded engine mounts. A complete set of flight and ground loads were applied to the test specimen, representing its entire spectrum multiplied by selected scatter factor. The safe-life approach was used to substantiate the engine mount to its durability requirements. The test program was launched on August, 2015, and finished on October, 2015, with application of ultimate loads after completion of cyclic testing. The dummy engine and the engine mounts are presented in Figure 15.

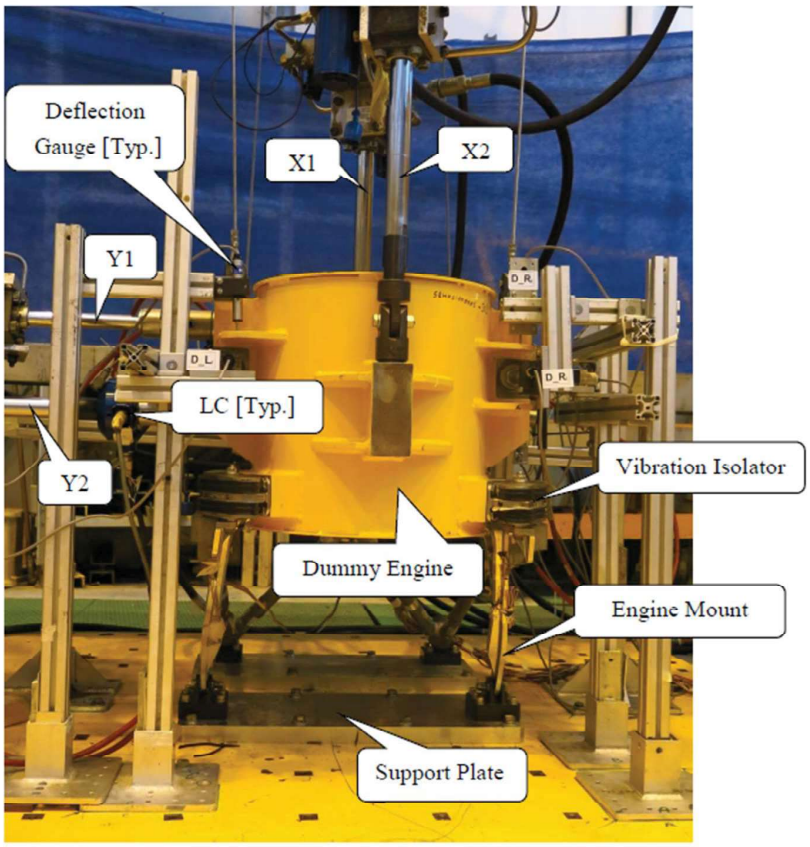

Figure 15. FMA IA-58H engine mount fatigue and static test setup

2.6 Determination of Safe Life Retirement Time of Helicopter Dynamic Components based on a Fretting Deterioration Model (O. Heit, N. Shemesh, K. Levi, V. Kalmanovich, IAF)

Standard helicopter dynamic components' fatigue retirement times are calculated based on Safe Life methodology, which derives the crack initiation analysis. This approach is appropriate for components operating under high frequency loads, in which a fatigue crack, if initiated, will grow and result in the component's failure in a matter of minutes or hours, therefore not allowing for non-destructive test intervals. Instead, the component must be scrapped when it reaches its calculated retirement time (CRT).

In this approach, the aircraft's usage spectrum, the component loading spectrum, and the component specific S-N curve (material and geometric properties), are combined together in order to account for the damage inflicted by each of the flight regimes. This damage is accumulated into the overall damage using the Miner Palmgren paradigm, and then translated into the calculated retirement time in terms of flight hours.

When a dynamic component is worn due to fretting, two failure mechanisms are usually observed. The first is surface chafing and the second is deviations from the nominal geometry. However, there are cases in which service fretting damage is found to be beyond what was observed in fatigue tests. A common method to deal with these cases is to analyze the geometric stress concentrations of the worn part in comparison to its nominal form. By reducing the S-N curve by the ratio of the worn and nominal stress concentrations, a new retirement time of the component is calculated. Recently, an Israel Air Force (IAF) S-65C-3 main rotor upper hub (see Image 1), showed severe spline teeth wear findings which were deeper than the manufacturer's fatigue test findings. It is assumed that these findings are due to severe usage which incorporates high frequency of torque cycles. The hub under these wear conditions was analyzed and the retirement time calculated was found to be inapplicable (less than 10 flight hours). Figure 16 presents the way the hub and the mast spline teeth interlock.

In light of logistic challenges and due to the impractical results, a fretting deterioration model was developed in order to calculate the component's retirement time which incorporates the temporary wear conditions. The logic of this model is illustrated in Figure 17. The implementation of this approach relies on wear measurements which were taken from different in-service hubs and were correlated with their accumulated flight hours using a curve fitting. The model, which progressively calculates the retirement time for the component, was developed, while accounting for the wear and subsequent damage it will experience throughout its service.

The Fretting Deterioration Model enabled to define a reasonable retirement time which can be implemented until new parts are purchased and installed in the fleet. The method had been made possible with the realization that the wear should not be considered as constant throughout the component life, and that the two mechanisms of fatigue and fretting are similarly time dependent, ultimately allowing for the expansion of the calculated retirement time.

This study was presented in the 56th Annual Conference on Aerospace Sciences [Ref. 3].

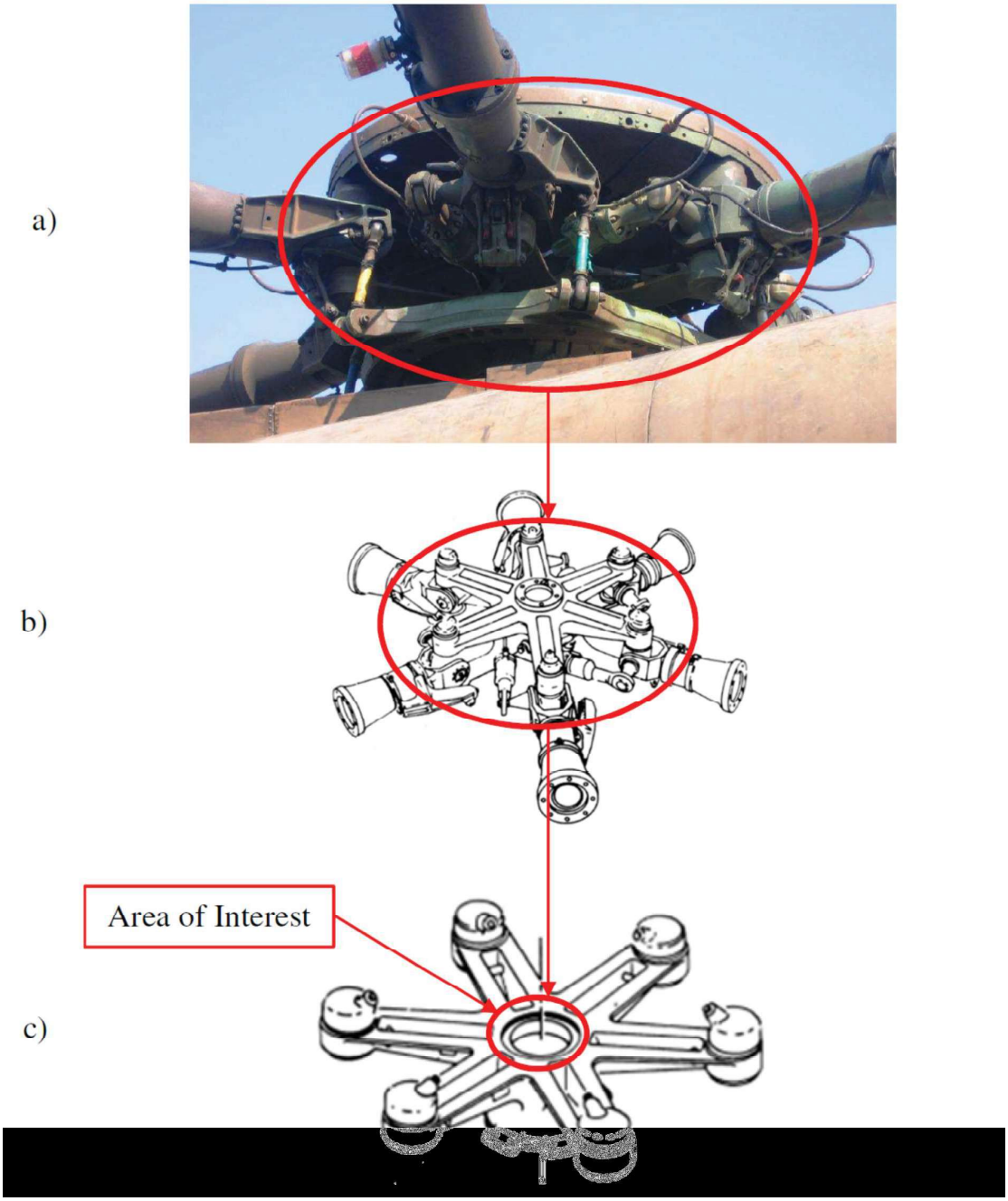

Figure 16. Main Rotor Upper Hub and Area of Interest: a) S-65C-3 Main Rotor, b) Main Rotor Upper Hub and Sleeves, c) Main Rotor Upper Hub Area of Interest

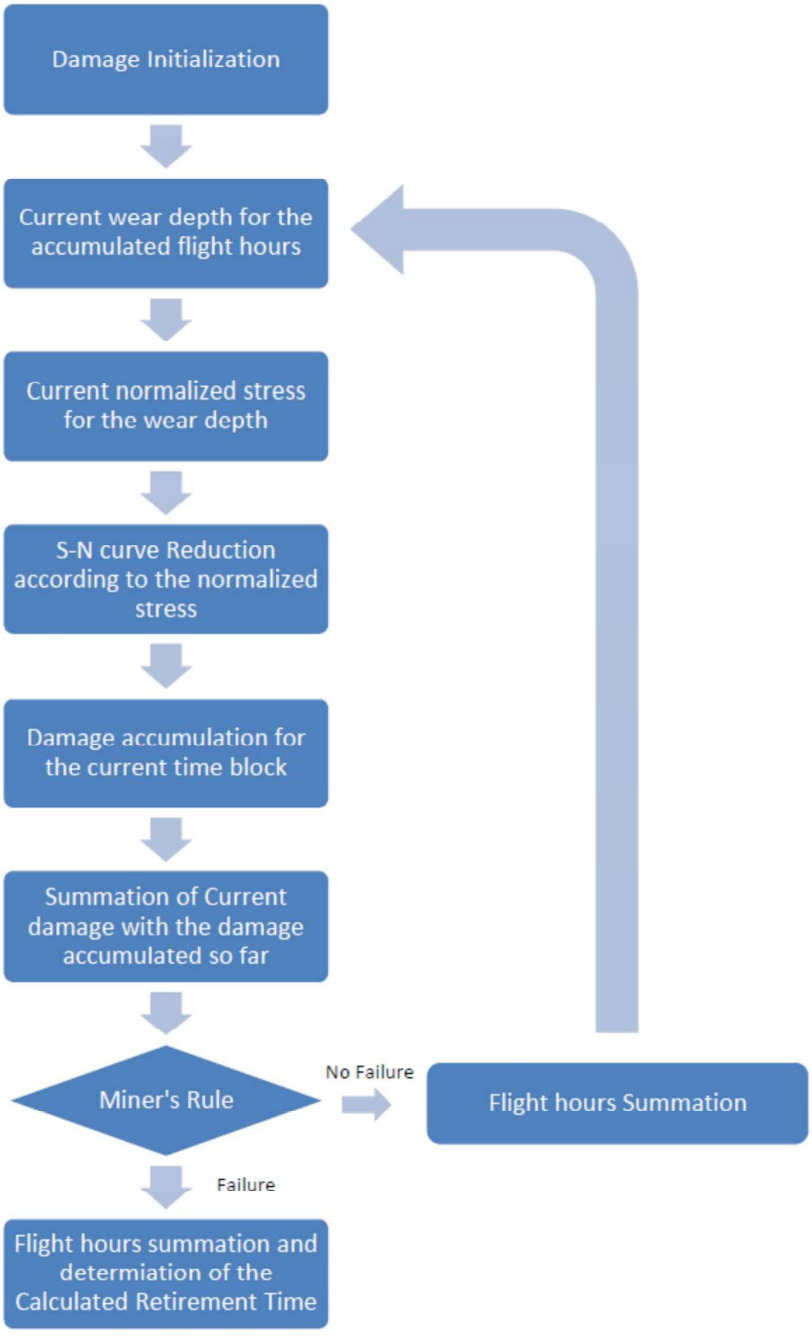

Figure 17. Fretting deterioration model concept

2.7 Fatigue Evaluation For Hi-Lok Fastener Installation Methods In Interference-Fit Holes (C. Matias, E. Katsav, IAI)

It is well established that structural joints using interference-fit fasteners will obtain longer fatigue lives as compare to transition-fit or clearance-fit fastened structures [4-7]. However, there is lack of information regarding the influence on fatigue lives for the different specific installation methods of the interference-fit fasteners.

Principal structural joints are usually composed of three structural member layers, and the fasteners are required to be installed in aligned corresponding holes. Examples of such principal structural members: double shear splice joints as attachments of two separate spar sections or double shear skin splices. The practical manufacturing of such joints using common assembly tolerances, introduces great deal of difficulties for interference-fit fastener installation (manufacturing usually struggle in installing the fasteners for such joints). Installing interference-fit fasteners in such joints can be achieved by either using methods of hand plastic hammering (as the preferred option), or by using pneumatic steel hammering.

Although proper installation of such fasteners should include controlled tapping of the pin head with a plastic mallet a light rivet gun", in fact, standard pneumatic steel hammer is commonly used in the assembly line. A concern was raised that such "violent" installation procedure might damage the holes such that fatigue advantages of these joints are questionable. Because of this concern and due to lack of relevant information, there is a tendency to design such joints to use transition-fit fasteners or even sometimes to use clearance-fit fasteners, and thus not benefit the fatigue advantages of interference-fit fasten joints.

The present study addresses this concern by performing fatigue tests accompanied with STRESSCHECK finite element [8] analyses, and fatigue analyses using "FATLAN" computer program [9].

There are many variables and parameters that influence the fatigue life of these structural members, such as: the interference-fit level, different level of load transfer (between the layers by the fastener), fastener clamp-up lever, fretting and friction between faying surfaces, or variable-amplitude loading. The present study purposely avoided including load transfer by the fasteners. This was done by uniformly induce the cyclic tensile loading into both layers of the tested specimen used. The tested specimen was design for best representing of such structural members. As a result, the following parameters and variables are examined in this study:

- The fastener fit level into a hole.
- The fastener installation method.

The study shows that common manufacturing practice of fastener-to-hole interference level using installation method of pneumatic steel hammering does not damage the holes, and the fatigue advantage of such joints is still appreciable. Significant improvements in fatigue lives

are being presented for interference fit fasteners installed via pneumatic steel hammering as compare to transition fit fasteners installed via plastic hand hammering (and the reference open-hole specimens). A clear relation of interference level to fatigue life is also shown. Higher interference levels contribute to higher fatigue lives even with using pneumatic steel hammering for the fasteners installation.

The test program includes specimens that are composed of two layers of AL7050-T7451 0.25" thick, attached by four 5/16 inch diameter titanium Hi-LoK fasteners of typical aircraft structure features and installation procedures. The specimens were manufactured and tested by the following four groups:

- Open hole specimens (2 AL7050-T7451 0.25" thick layers) used as reference base-line.
- Specimens having transition-fit installed fasteners by hand plastic hammering.
- Specimens having interference-fit installed fasteners by hand plastic hammering.
- Specimens having interference-fit installed fasteners by pneumatic steel hammering.

Total of 13 specimens were tested (26 plates 0.25" thick) composed of 4 specimens of group "A", and 3 specimens for each of the other groups. The specimen were fatigue tested using constant amplitude tensile loading at R=0.05 and peak stress of 16.1 ksi. In addition, each 500 cycles block (of the loading specified above) was followed by 5 cycles of about 20% higher loading, which served as a "simple" set of load markers to be used in detailed fractographic analysis of the failed specimens.

Figure 18 presents the specimen fasteners installation procedure, tooling used for the installation procedure and examples of testing via the tensile machine. Figure 19 and Figure 20 present representative test results. Figure 19 presents a Group B specimen test results (Specimen having transition-fit installed fasteners by hand plastic hammering) showing specimen failure due to cracking at fastener holes. The fatigue life and cracking scenario is quite similar to the results presented by the reference specimens of the open hole. Figure 20 presents a Group D specimen test results (Specimen having interference-fit installed fasteners by pneumatic steel hammering) showing specimen failure due to cracking at the testing machine clamping jaws as the primary damage, and secondary cracking near fastener holes but not at fastener holes. No cracks were developed from any fastener hole. This clearly shows that specimens Type D fastener holes have significant lower stress concentration factor then the stress concentration factor related to the serrated clamping jaws "hard point" (of the tensile machine) and that of specimens Type B & A. The fatigue lives of the specimens of Group D were significantly higher than that of type A and B specimens.

More details on this study are provided in Ref. 10.

Figure 18. Specimen fasteners installation procedure, tooling and testing via the tensile machine

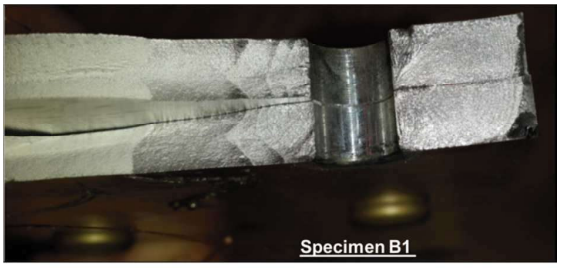

Figure 19. Specimen having transition-fit installed fasteners by hand plastic hammering test results

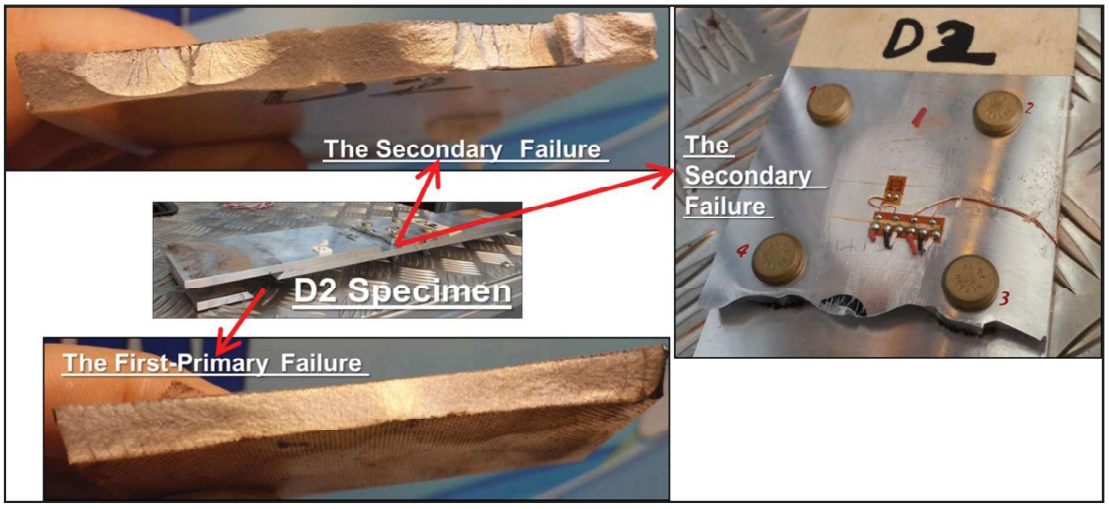

Figure 20. Specimen having interference-fit installed fasteners by pneumatic steel hammering test results

2.8 Influence of Thickness and Hole Diameter on Mutual Interaction of Two Opposing Cracks at a Hole (C. Matias, Y. Amran, IAI)

Holes in the structure are typical locations prone to fatigue cracking. Usually cracks will develop at both sides of a hole, such that for some period the two unequal opposing cracks, might grow simultaneously, interact and influence each other. This mutual interaction is such that the larger crack influences the smaller one so that it will accelerate to "catch-up" and have a tendency to equal its length to the larger crack. In turn, the smaller crack influences the larger to accelerate it, but by lower factors (that are not negligible). Comparing crack growth life analyses results for accounting of these mutual interactions vs. not accounting, by ratio the results for the "not accounting" to the "accounting", reveals crack growth life ratio factors that range from 1.3 for common structural configurations and up to a factor of 2 for infinite

width dimensions. These results certainly mean that this mutual interaction effect cannot be ignored in analyses as it has significant impact on the cracking growth lives.

This current study makes use of the state-of-the-art NASGRO computing code [36] in evaluating the two opposing cracks initiated from the same fastener hole mutual interactions. The hole diameter impacts this mutual interaction of the two opposing cracks that grow out of it. In addition, the thickness in which cracks are growing presents significant impact on mutual interaction of two opposing corner cracks at a hole (part-through-the-thickness cracks). The thickness and the hole diameter parameters are being evaluated for their influence on the mutual interaction of two opposing cracks at a hole. Test results for two opposing cracks at a hole were examined. The cracking growth data is acquired by Fractographic analyses done on coupon tests and is accompanied by cracking growth analyses that includes mutual interaction effects. A common cracking growth scenario analyzed includes of a primary crack accompanied by a secondary crack growing at the other side of the hole. Each crack affects the other tip Stress Intensity Correction Factor (SIcF). NASGRO computer code uses solution for this mutual interaction of two opposing unequal cracks at a hole under remote tension loading. That solution is based on solution that was presented by Tweed and Rooke [37]. The Tweed and Rooke solution involves solving coupled singular integral equations by numerical method. The original Tweed and Rooke solution is computationally too intensive to be used as is in a code. The National Research Institute of Canada (NRC) developed several closed-form solutions [38] to approximate the Tweed and Rooke solution. The latest Canadian NRC solution is the one implemented into the NASGRO computed code.

Figure 35 presents SIcF, for through-the-thickness cracks of a single and of two opposing cracks at a hole, in an infinite width plate. The blue continues curve presents data for the primary crack, and the red continues curve presents data for the secondary accompanying crack, both per an analysis that accounts for the mutual interaction. The doted curves of blue and red present data for a single crack growing from a hole (no mutual interaction).

The following data trends are observed:

(1) The SIcF of the smaller crack is influenced by the opposing larger crack for its entire growth

(2) The SIcF of the larger crack is starting to be influenced by the opposing smaller crack for above 3% level, only for crack lengths larger than 60% hole diameter (and the influence of the smaller opposing crack is dramatically getting higher as the smaller crack grows)

(3) As both smaller and larger opposing cracks grow, their lengths become getting equal and the SIcF for each one of them, is getting to be equal to 1.0 (two opposing large cracks at an infinite width are accounted as one crack with no hole).

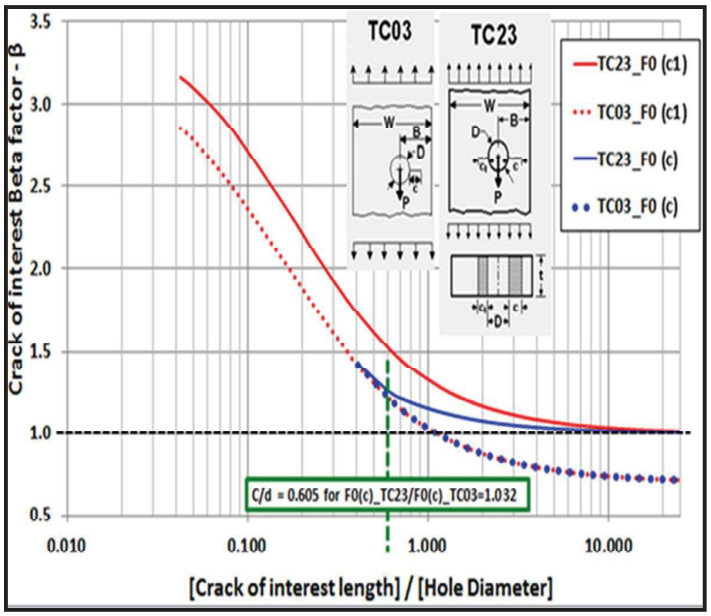

Figure 21. Stress intensity correction factors for single and two opposing cracks at a hole in an infinite width plate.

Figure 22 and Figure 23 present SIcF data for the mutual interaction as function of crack length normalized to hole diameter. Figure 22 is for the influence of the large crack on the small crack, and Figure 23 vice versa. Figure 22 and Figure 23 present also the opposing cracks length ratios along the cracking growth. The following data trends can be observed:

(1) Starting with unequal two opposing cracks (1:10 length ratio) ends up with equal length for the two opposing cracks

(2) As the two opposing cracks grow the mutual interaction becomes higher (For influence of large crack on small crack starting from about 1.1 influence factor, and getting to an upper "limiter" influence factor of about 1.42. For influence of small crack on large crack starting from about 1.0 influence factor, i.e. no influence, and getting to an upper "limiter" influence factor of about 1.40).

Note: the SIcF presented data are for through-the-thickness cracks.

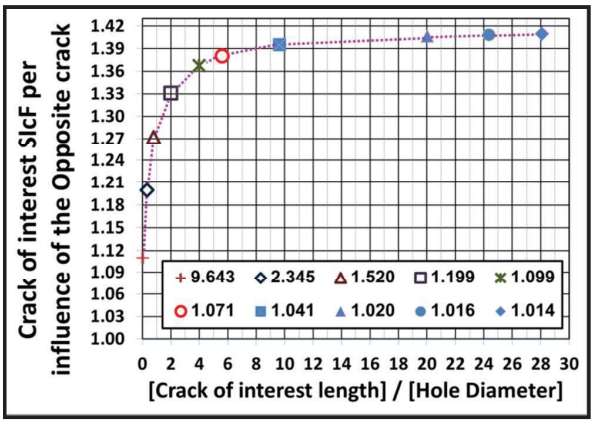

Figure 22. Stress intensity correction factors for influence of large crack on small crack in a hole.

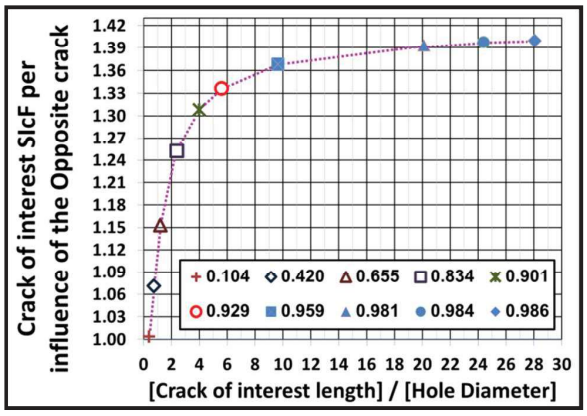

Figure 23. Stress intensity correction factors for influence of small crack on large crack in a hole.

Evaluation for effects of thickness in the presence of part-through-the-thickness cracks (as corner cracks) and different hole diameters, reveals that the trends as presented above are being kept, but with slight differences that are enough to cause significant impacts on crack growth life.

As the mutual interaction between two opposing cracks at a hole is higher, the crack growth life ratio (of analysis not accounting for mutual interaction over analysis accounting) is higher.

Figure 24 presents analyses crack growth life ratios for not accounting of mutual interaction over accounting, as function of thickness and 3 hole diameters: 0.125", 0.2" & 0.44". The data includes analyses for through-the-thickness cracks and for corner cracks. The following is observed:

(1) Life ratio of through crack is higher relative to corner crack

(2) As plate thickness is larger (corner cracks), life ratio is lower (per hole diameter, ratio gets to a constant)

(3) As hole diameter is larger, life ratio is lower (corner & through cracks)

(4) For infinite width (primary & secondary initial cracks of 0.05" & 0.005"), life ratio ranges from factor of about 2 to about 1.2

(5) Per hole diameter, the maximum reduction in life ratio per thickness variation, is about 26% - 27%.

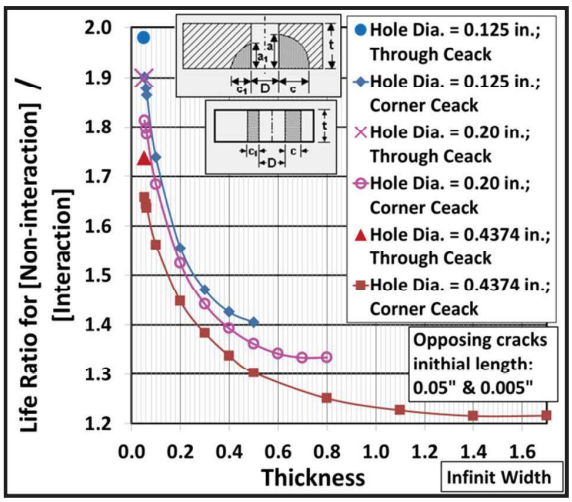

Figure 24. Analysis life ratio of [Non-interaction]/[Interaction], per thickness and hole diameter.

2.9 On the integrated fatigue design method (M. P. Weiss, Technion)

The fatigue research has been traditionally divided into two very different approaches. One is the "Fatigue Life Methodology" which is based on the extensive test results that have been accumulated during the 180 years of fatigue testing. The main fatigue terms used in this methodology are: *Endurance limit, Wohler curve, Miner's rule, Probabilistic approach*, and many others. The second approach is the "Damage Tolerance Methodology" that is based on behavior of cracks and on fracture mechanics. The terms used in this methodology are: *crack initiation, crack propagation, SIF - stress intensity factor, SIF threshold, fracture toughness, J integral* and many others.

Most fatigue problems are encountered in industry and in aeronautics. The designers have to select which fatigue design approach is better for their problem. In industry the designers' knowledge in the field is often insufficient. In aeronautics the accepted design rules are

obviously more stringent, but also not too reliable. The requirement to choose the appropriate fatigue design method by designers, in spite of their limited knowledge, is unacceptable.

The author tackled the problem and tried to develop an integrated fatigue design methodology that will combine the two approaches, namely the "Fatigue Life Methodology" and the "Damage Tolerance Methodology", and will enable designers to use clear path in their fatigue design without the need to select one of two. The first general idea how to combine the approaches has been published in the ASME Engineering Materials Journal in 1977 [39] as a speculation. A first quantified study was published in the International Journal of Fatigue in 1992 [40]. The method was further developed, as is customary in research and several more advanced studies have been published in prominent Journals and presented in conferences. Finally the latest integrated method has been published in the International Journal of Fatigue in 2016 [41], and is shortly described here.

The concept of the integrated fatigue design method is calculating step by step crack propagation from the onset of loading till failure. The calculation is performed in each combination of crack (or even tiny micro crack) length and any stress amplitude. The simulation is explained on the Fatigue Diagram and performed using dedicated software, and the results can be seen on the following diagram. The method is detailed in Ref. [41].

The Fatigue Diagram shown in Figure 25, divides the whole Fatigue Domain into 6 zones, each zone includes a certain fatigue mechanism, or a combination of mechanisms, and any combination of crack length and stress amplitude enables to calculate the following next step propagation, according to the calculation method that fits to the relevant zone. The propagation steps are cumulated till failure.

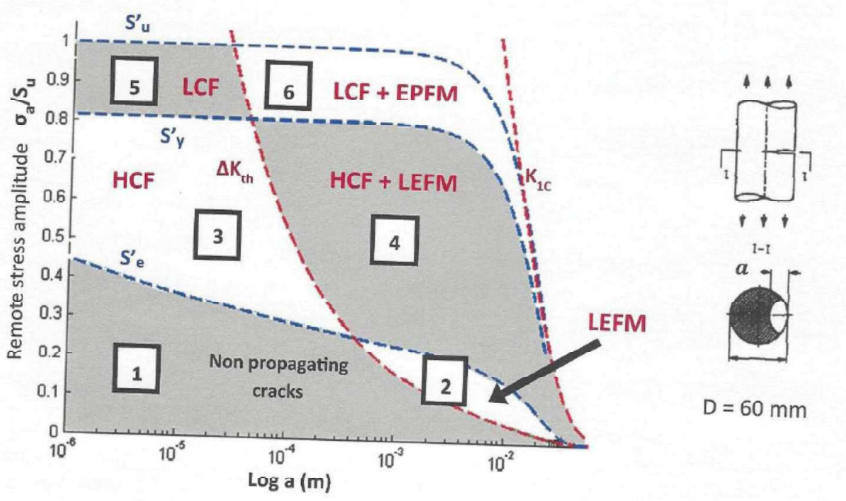

Figure 25. Fatigue diagram proposed by M. P. Weiss.

2.10 Research activities in Ben Gurion University – Mordechai Perl Group (M. Perl, BGU)

Prof. Mordechai Perl from Ben Gurion University (BGU) and his co-workers were focused on different aspects of fracture mechanics related to pressure vessels in general, and to the process of autofrettage specifically. The effect of the Bauschinger effect on the stress intensity factors, especially for three dimensional problems, was investigated as well [42-49]. The three dimensional analysis presented in these publications was performed by means of the finite element method, implementing a novel realistic autofrettage residual stress field (that also incorporates the Bauschinger effect). The stress intensities were evaluated for different combinations of radial and coplanar cracks of different depth to wall thickness ratios. An example of such stress intensity factors is provided in Figure 25.

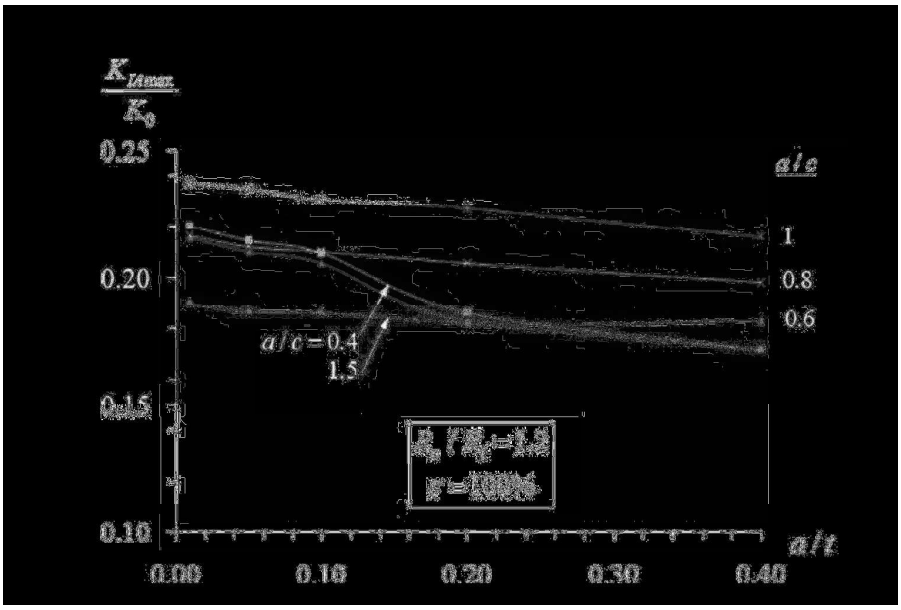

Figure 26. Stress intensity factor variations for different elliptical cracks dimensions in fully autofrettaged vessels with relative thickness R_o/R_i = 1.2.

3. STRUCTURAL INTEGRITY OF COMPOSITE MATERIALS

3.1 Implementation of Invariant-Based Approaches for Determination of Composite Materials Allowables (Y. Freed, IAI)

Composite materials are characterized by high stiffness to weight ratio, can be tailored to a specific load conditions, and are relatively easy to shape for complex contours. When produced in serial productions, they can be cost effective even though their price is higher than metals. Their potential for weight saving was identified by the aviation industry long ago. Today, the maturity of the fabrication procedures with the constant reduction in costs encourages more and more manufacturers in the aviation industry to consider using composite materials for primary structures, and most recently developed airplane models have an appreciable amount of structural components made of composite materials. For example, the Airbus A350 and the Boeing 787 models have both more than 50% of their structural components (in terms of weight) made of composite materials.

This process of substantiating the structural performance and durability of composite components generally lies on the building block approach, shown in Figure 27. It is well understood that testing alone can be very expensive because of the number of specimens needed to verify every geometry, fabrication process, loading, environmental condition and failure mode. Analysis techniques on the other hand, are usually not accurate enough to adequately predict results under every set of conditions. However, extensive use of analytical predictions (based on finite element modeling) that are validated by test can reduce the overall cost of the program without reducing reliability or affecting the airframe structural integrity.

The Building Block approach is a widely used, logical and systematic method that is employed for substantiation of composite structure during development programs. It consists of three main stages (marked as 'Groups' A to C in Figure 27), that defines the testing level from the coupon level up to full scale. Though it is recommended to apply this procedure from Block 1 up to Block 6, in the real world, preliminary design and analysis of parts, elements and subcomponents is usually accomplished using preliminary or estimated material allowables. This is due to the relatively long period of the material property development phase. However, material allowables should be fully determined before full-scale component testing starts.

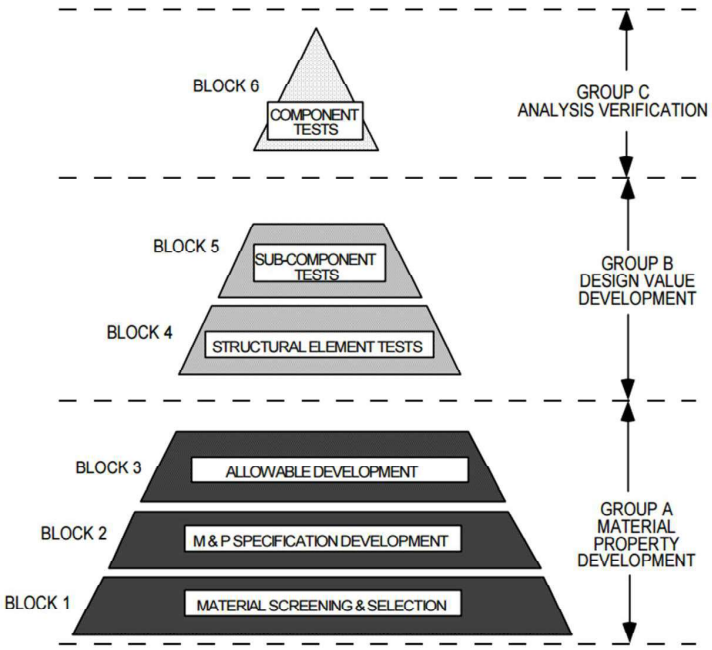

Figure 27. Building Block Approach (taken from Ref. [11]).

At the lowest Building Block level (Group A – material property development), small coupon specimens and element tests are carried out to characterize basic unnotched and notched static and fatigue material properties under different environmental conditions. The test sequence shown in Figure 28 is usually employed to each material system at certain environmental condition, for a certain laminate stack-up and loading condition. The use of six panels made of three different material batches is aimed to cover any uncertainties related to material and process scatters, and provides the engineer sufficient test data for statistical analysis. It is understood that a development program that covers all failure modes, environmental conditions and material stack-ups can be summed up to thousands of test specimens.

The objectives of Group B are to develop design values that reflect the actual structure. This is higher level than the material level, and accounts for geometry properties, interaction between adjacent elements and issues and uncertainties that may be raised during assembly. Usually these tests are conducted at relatively early stage of the development program and are considered mainly for risk mitigation. As a result, the specimens are sometimes characterized by preliminary configuration with general sizing.

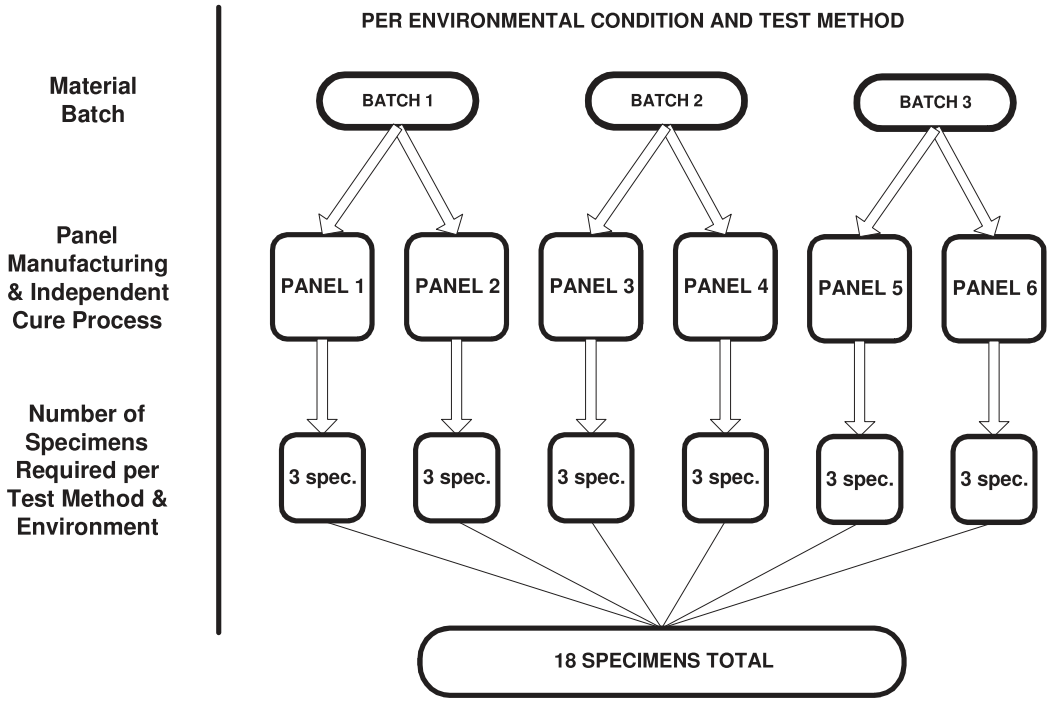

Figure 28. Typical coupon test matrix for determination of B-Basis material allowables.

The final stage of the building block approach is Group C, in which full scale tests are conducted and used for the certification process for static and fatigue substantiation. At this level, it is desirable to perform extensive validation of the analysis tools that were used during the design.

It may be noted that sometimes not all blocks described in Figure 27 are accomplished during the development program. In its simplest form, the building block approach represents a method of risk mitigation (both technical and financial). Testing at the various levels reduces the probability that significant surprises will materialize near the end of a program. The certification authorities do not require the applicant to demonstrate accomplishment of all blocks, but are focused on testing in Group A and C levels as described Figure 27.

Analytical approaches to reduce the amount of required testing in the material level are constantly investigated. These methods are usually required determination of mechanical properties in the micro level, such as fiber and matrix moduli and strengths (Refs. [12-15], among many others). In this study, the 'trace method' and 'Omni Strain Failure Envelope' suggested in Refs. [16] and [17] are employed for determination of stiffness and strength properties of composite materials. The 'trace method' provides and easy to use guidelines for this purposes. As discussed in the full length paper (Ref. [18]) and presented here in Figure 29, this method provides excellent predictions for stiffness properties of various Carbon and Kevlar based composites after modified slightly in light of IAI in-house material properties database. However, the 'Omni Strain Failure Envelope' method was found to be very conservative for determination of strength properties.

Figure 29. Predictions of transverse Young's modulus versus test results for different Carbon and Kevlar based composites.

3.2 On the scatter factor in fatigue testing of composite material structures (D. Elmalich, Y. Freed, IAI)

Composite materials are widely used in the aviation industry in recent years. Among their advantages are their superior fatigue characteristics. While the Federal Aviation Regulations for transport category airplanes does not distinguish metallic structural parts from composite material ones, the current industry practice is to employ the guidelines provided in Ref. [11] for certification purposes of structures made of composites. According to Ref. [11], the airframe should be substantiated by tests or analysis supported by test evidence. Since large scale tests are conducted on a single test article, possible scatter due to material and manufacture variability must be accounted for by means of application of scatter factors on the design life goal of the product. It is commonly agreed that the scatter in composite materials is greater than that of metals.

The first comprehensive study on scatter in composite materials was conducted by Northrop-Grumman back in the 1980s as part of the Navy F-18 development program (Ref. [19]). In this study, several structural details and variables such as laminate lay-up, loading mode, load transfer, specimen geometry and environmental effects were accounted for in tests. This program included autoclaved 350˚F-cure graphite-epoxy composites, and the analysis was conducted primarily on fiber-dominated failures. The concluding remarks were to employ scatter factor of 13.3 on the lifetime of the composite structure. To avoid the high costs involved in executing such long tests in the development program, Whitehead and his co-workers suggested employing a Load Enhancement Factor (LEF) that increases the damage during test, and can be adjusted to the desirable scatter by means of mathematical manipulations (Ref. [19]). For instance, application of LEF = 1.15 with 1.5 lifetimes in test is equivalent to a scatter factor of 13.3. Note that application of large load enhancement factor can change the failure mechanism of the composite and provides unrealistic failure predictions; therefore, a certain caution should be taken when applying the LEF. This concept is even more problematic if the test article includes metallic parts. Application of load enhancement factor can cause unrealistic retardation effects and the performance of these metallic parts in fatigue test cannot be validated properly. More details on this concept are provided in Refs. [25] and [26].

Although fatigue life is very sensitive to the presence of damages, the scatter in testing (both static and fatigue) actually reduces in the presence of initial flaws in the test coupons (Ref. [20]). This phenomenon is explained by the fact that the stress concentration in the notched composites is the main driving force for the final failure of the specimen, while for intact specimens the failure can initiate in various locations in the test specimen. The choice of intact test specimens in Northrop-Grumman study (Ref. [19]) is somehow a drawback from design point of view, since the current regulations requires to design the composite structural detail to a 'no growth' criterion. According to this criterion, the test specimens used for determination of material allowables consist of certain damage or flaw (usually open hole specimens are tested), which reflects possible damage (manufacture or service) in the structural detail. Consequently, the material scatter in fatigue should be considered for

damaged coupons rather than intact, and is expected to be lower than that determined in Ref. [19].

This statement was further demonstrated in Refs. [20]-[23], in which the scatter factor in fatigue of composite materials was found to be much lower than that determined in Ref. [19]. The objective of this study is to recommend on a scatter factor to be used for fatigue testing. A comprehensive test plan was established for several material systems manufactured by wet layups and prepregs. The material systems that have been tested are glass, carbon and Kevlar based composites. The test specimen included open-hole, disbonding and impact flaws. The Modified Joint Weibull approach (Ref. [24]) was employed as the statistical basis for determination of scatter parameters.

The statistical Weibull shape parameter, β_L, the life factor, N_F, the Weibull shape parameter, βr, the load factor, SF, and the life-load factor N_0 were obtained for the 25 specimen configurations. All data is presented in Ref. [27]. The life factor and the load factor are calculated as B-Basis values assuming that only one sample of component test is carried out (i.e., a single full scale test article). The Weibull shape parameters, β_L and β_r are calculated based on the final failure of the coupon specimens of each material system rather than the first ply failure. While the fatigue life Weibull shape parameters, β_L, is calculated from coupon test results for each material system, the corresponding fatigue load Weibull shape parameter β_r is considered constant and equal 20. Since the scatter of the static residual strength of run-out specimens (comply with the no-growth concept that is adopted) is very close to that of the static test specimens, a value of $\beta_r = 20$ is considered conservative. For example, the average of β_r values calculated for materials Glass #1, #2 and Kevlar #1 is about 35. The data gathered from the tests of the 25 configurations is examined for the following parameters: scatter by material system, scatter by type of flaws (disbonding, open hole and impact), and scatter by manufacturing process (wet lay-up vs. prepreg).

Averages of the Weibull shape parameters with respect to the 3 grouping approaches and the corresponding fatigue life factor are shown in Tables 2-4. An averaging of the Weibull shape parameter β_L with respect to the three materials tested and the corresponding fatigue life factor is presented in

Table 1. It is observed that the fatigue life factors for both Carbon fiber based materials and glass fibers based material systems are relatively low, much lower than the traditional fatigue life factor of 13.3. In that sense, the Kevlar fiber materials, which present inferior scatter characteristic with respect to Carbon fiber and glass fibers, also present better scatter characteristics than the traditional ones presented in Ref. [19].

Material system	β_L	N_F	SF
Glass	4.780	1.845	1.16
Carbon	4.247	2.000	1.16
Kevlar	2.413	3.550	1.17

Table 1. evaluation of fatigue life scatter parameters grouped by fibers material

Results of averaging the Weibull shape parameter β_L with respect to the specimen types and the corresponding fatigue life factor are shown in

Table 2. Some of the material systems that involve sandwich configuration reveal wide scatter. However, these deviations are attributed to the complexity of the determination of fatigue life in the sandwich specimens. This complexity lies on the fact that the fatigue life for the sandwich specimens should be determined from the time that the flaw buckles to global failure of the specimen. This is difficult to track during cyclic test and requires multiple breaks during test to closely validate if the flaw has propagated or not. It should be noted that despite the deviations in some of the sandwich specimens, the average scatter factor obtained for this type of specimens was still much lower than that reported in Ref. [19]. In the case of the impact flaw specimens, on top of the complicated determination of the failure propagation, the fatigue life scatter is affected by the inconsistent geometry of the flaw. While a consistent energy level is applied to the test specimen to form impact damages, the corresponding impact flaw dimensions due to this energy have certain variability between different coupons. Yet, here also the fatigue life scatter is lower than the one reported in Ref. [19]. As expected, not much scatter was reported for open hole specimens.

Specimen type	β_L	N_F	SF
Open-hole (solid laminate)	5.745	1.657	1.16
Disbonding flaw (sandwich)	3.026	2.701	1.16
Impact flaw (sandwich)	2.158	4.177	1.17

Table 2. Evaluation of fatigue life scatter parameters grouped by specimen type

The last aspect that has been examined is the manufacturing process.
Table **3** presents the average Weibull shape parameter β_L and the corresponding life factor for wet lay-up and prepreg lamination. It is well observed that the fatigue life scatter factor for both manufacturing processes is very low (also here, some deviations are observed in the sandwich panels specimens). Surprisingly, the wet lay-up provides better scatter than that of prepreg manufacturing process.

Manufacturing process	β_L	N_F	SF
Wet lay-up	5.148	1.762	1.16
Prepreg	2.876	2.854	1.16

Table 3. Evaluation of fatigue life scatter parameters grouped by manufacturing process

Figure 30 summarizes the relation between the test duration and the load enhancement factor. The solid thick line represents the authors recommend curve for the LEF factor. It reflects test duration of 3.5 lifetimes with no load enhancement factor applied. This curve covers all of the examined groups aside from the grouping by impact specimens, which was explained earlier that is somehow problematic for material scatter determination. Entering the vertical axis with the required load enhancement allows retrieving the corresponding component test duration. For example, LEF of 1.02 (which represent a 2% increase to the applied loads) shortens the component test duration from 3.5 lifetimes to 3.0 lifetimes.

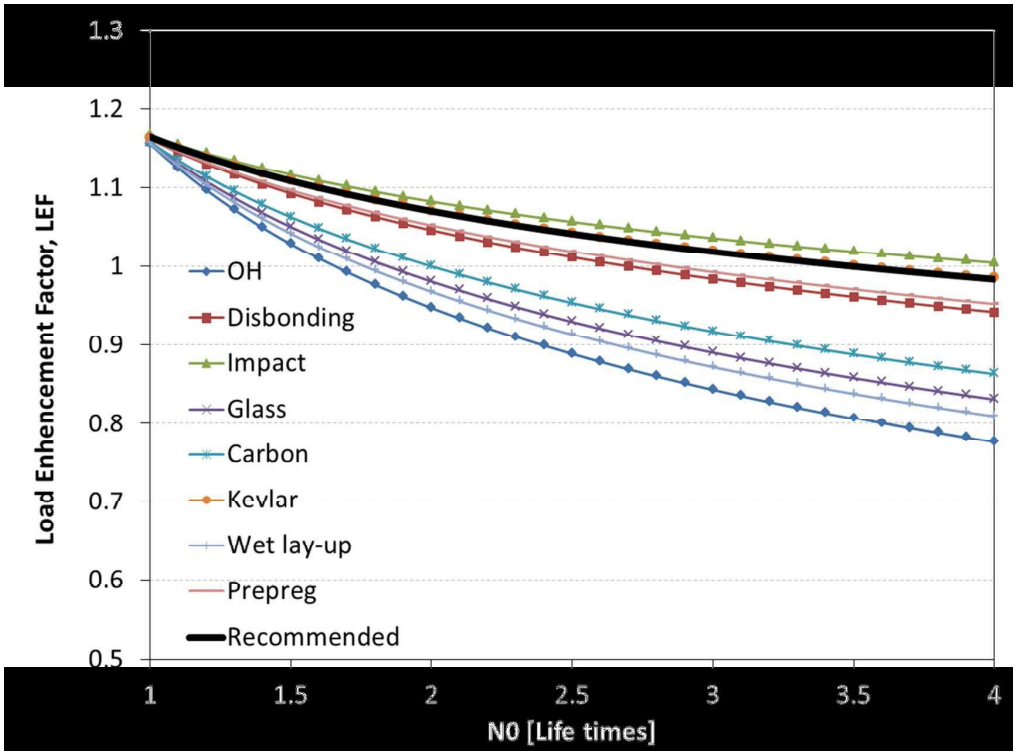

Figure 30. Life enhancement factor versus component test durations per grouping approaches.

3.3 Examination of the KAWAI CLD Method for Fatigue Life prediction of Composite Materials (Y. Buimovich, D. Elmalich, IAI)

The use of advanced composite materials in aircraft primary structures has been significantly increased over the past 25 years. Modern large commercial aircraft are designed with more than 50 percent composite materials, due to the demand for fuel-efficient, light-weight, and high-stiffness structures that have fatigue durability and corrosion resistance [22,25]. It is well known that aircraft structures are subjected to complex fatigue loading that accompanies changes in the amplitude, mean, frequency and waveform of stress cycling during service. Apparently, a large number of fatigue tests under different kinds of cyclic loading conditions is required to elucidate the effect of loading mode on the composites sensitivity to fatigue; thus, this consumes considerable time and cost. Therefore, a time and cost-saving procedure for identifying the loading mode dependence of composites fatigue strengths is required. This procedure should assure reasonable accuracy on the basis of a minimal amount of test data.

The KAWAI CLD [50,51] is a Constant Life Diagram (CLD) method that has been examined in IAI for fatigue life predictions of composites. In this method, fatigue tests are carried out at one critical R-ratio, defined as the ratio of the Ultimate Compression Strength (UCS) over Ultimate Tensile Strength (UTS) of the material. This critical ratio is called χ. This method is a time and cost-saving procedure that provides reliable data, as compared to the linear Goodman curve, that its use for composites does not reflect the actual behavior of the material [50-52].

Static and fatigue tests were carried out for open-hole coupon specimens made of unidirectional carbon/epoxy tapes for examination of the applicability of the KAWAI modified constant life model. A quasi-isotopic lay-up of intermediate modulus unidirectional (UD) Carbon/epoxy tapes was examined. The lamination sequence, [(+45°, 90°,-45°, 0°)s]s, is balanced and symmetrically stacked. The geometry of the specimens was in accordance to ASTM standard for open-hole tests (ASTM D5766, ASTM D6484). The specimen is illustrated in Figure 25. A total of 56 composite specimens are tested. The tests included static compression and tension strength to obtain the critical R ratio. Fatigue testing included five R ratios; i.e., 0.5, 0.1, χ, -1 and -10. Most R-levels consisted of five levels of stresses (with two tests at each stress level).

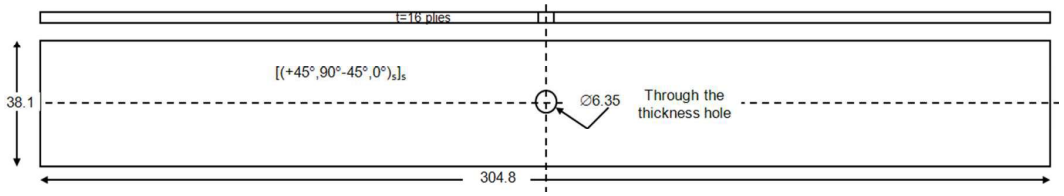

Figure 31. IM Carbon UD/ER450 Open-Hole Tension and Compression Specimen for Quasi-isotropic lamination

The critical R-ratio obtained from the static tests is χ=-0.5. Hence, CLD was built based on the fatigue tests results for R= χ. The predicted CFL and test results of fatigue tests are shown in Figure 32. Note that the values of the mean and amplitude stress in
are normalized with respect to the reference stress σ_b. A relatively good agreement Figure 32 was obtained between the predicted and experimental results, with the exception of R=-10. More tests are currently conducted to improve the accuracy of the CLD model. It may be further noted that according to test results, the Goodman curve highly overestimates fatigue life for purely tension and tension-compression areas and underestimates fatigue life for R-ratios lower than R=-1.

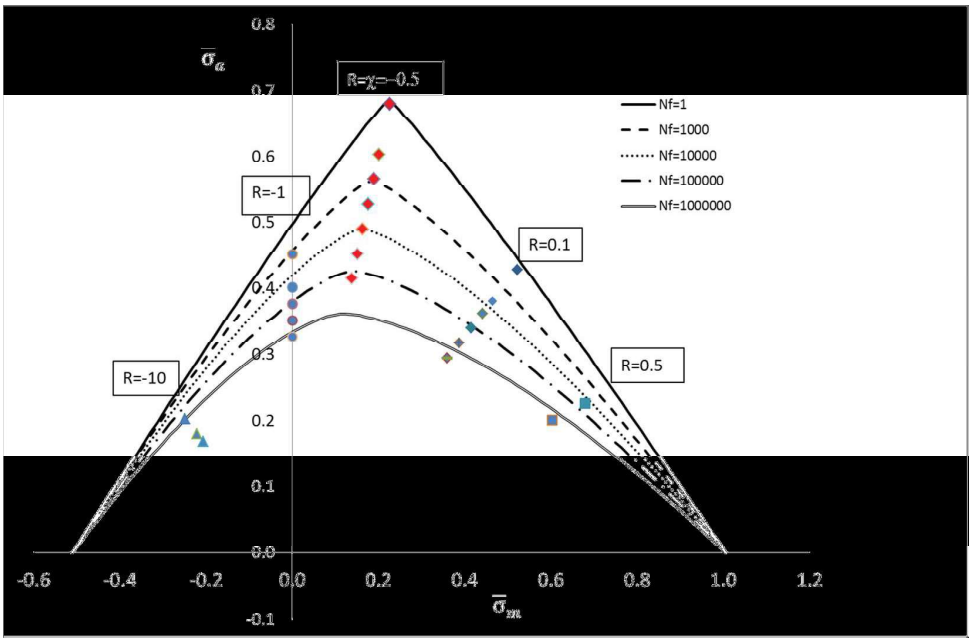

Figure 32. Constant Fatigue Life Diagram for unidirectional Carbon/epoxy laminates

3.4 Research activities in Weizmann Institute Composite Materials Laboratory (D. Wagner, Weizmann Institute)

The research at the Weizmann Institute Composite Materials Laboratory, leaded by Prof. Daniel Wagner, focuses on several themes: The interfacial adhesion and fracture physics in polymer composites (micromechanics and nanomechanics); the nanomechanics of carbon and non-carbon nanotubes and nanocomposite materials; the stress-sensing potential of carbon nanotubes in polymer matrices; and the relationship between (micro, nano) structure and mechanics in biological composites. The main emphasis and common thread between the various projects is the uncovering of phenomenological and mechanical similarities between apparently different materials families possessing common fibrous characteristics. A secondary focus is on two-dimensional microstructures - surfaces, interfaces, and interphases – which have a profound influence on the physics and mechanics (stress transfer, deformation,

fracture) of fibrous composites of any kind, synthetic and natural. Applications for synthetic composites range from re-entry heat shields for spacecraft, new aircraft designs (such as the Airbus 380 and Boeing 787), fishing rods, tennis racquets, bicycle frames and racing car bodies, solar panel substrates, and orbital telescopes.

In Ref. [53], the effect of the filler geometry on the toughness, the strength and the stiffness of the composite material were investigated. The particular cases of nanotubes, thin wall general cylindrical fillers, and thin ribbons were examined. The study revealed how the properties of nanocomposites can be optimized by modulating the filler shape and dimensions, as well as the mechanical properties of the material and interface. The tradeoffs between toughness, strength and stiffness were analyzed in view of their different and sometimes opposite dependence on the material and geometric parameters. It was shown that when the filler is shorter than its critical length, typical of most current nanotubes, the toughness, strength and stiffness can be improved simultaneously by reducing the filler cross-sectional aspect ratio (wall thickness divided by diameter). The mechanical performance of composites reinforced by carbon nanotubes and microfibers is compared for several possible filler packing conformations, demonstrating the high potential of nano reinforcement, as depicted in Figure 33.

The demonstration of the potential of nano-reinforcements was furthered demonstrated in Ref. [54], in which The strength and adhesion properties of individual CNTFs in epoxy were measured by continuously monitored fragmentation tests and characterized by electron microscopy. A theoretical model was applied to account for the nanotubes unique cross-sectional geometry, comprising millions of individual multi-walled Carbon nanotubes, and for the effect of matrix penetration. The composite strength and toughness were found to be strongly dependent on and improved by the extent of penetration, suggesting that the composite mechanical properties would be tunable by controlling the interphase.
In Ref. [55], it was shown that the fracture toughness of single-walled nanotubes (SWNTs) conforms to the classic theory of fracture mechanics, even for the smallest possible vacancy defect (~2 Å). By simulating tension of SWNTs containing common types of defects, it was demonstrated how stress concentration at the defect boundary leads to brittle (unstable) fracturing at a relatively low strain, degrading the ideal strength of SWNTs by up to 60%.It was found that, owing to the SWNT's truss-like structure, defects at this scale are not sharp and stress concentrations are finite and low. Moreover, stress concentration, a geometric property at the macroscale, is interrelated with the SWNT fracture toughness, a material property.

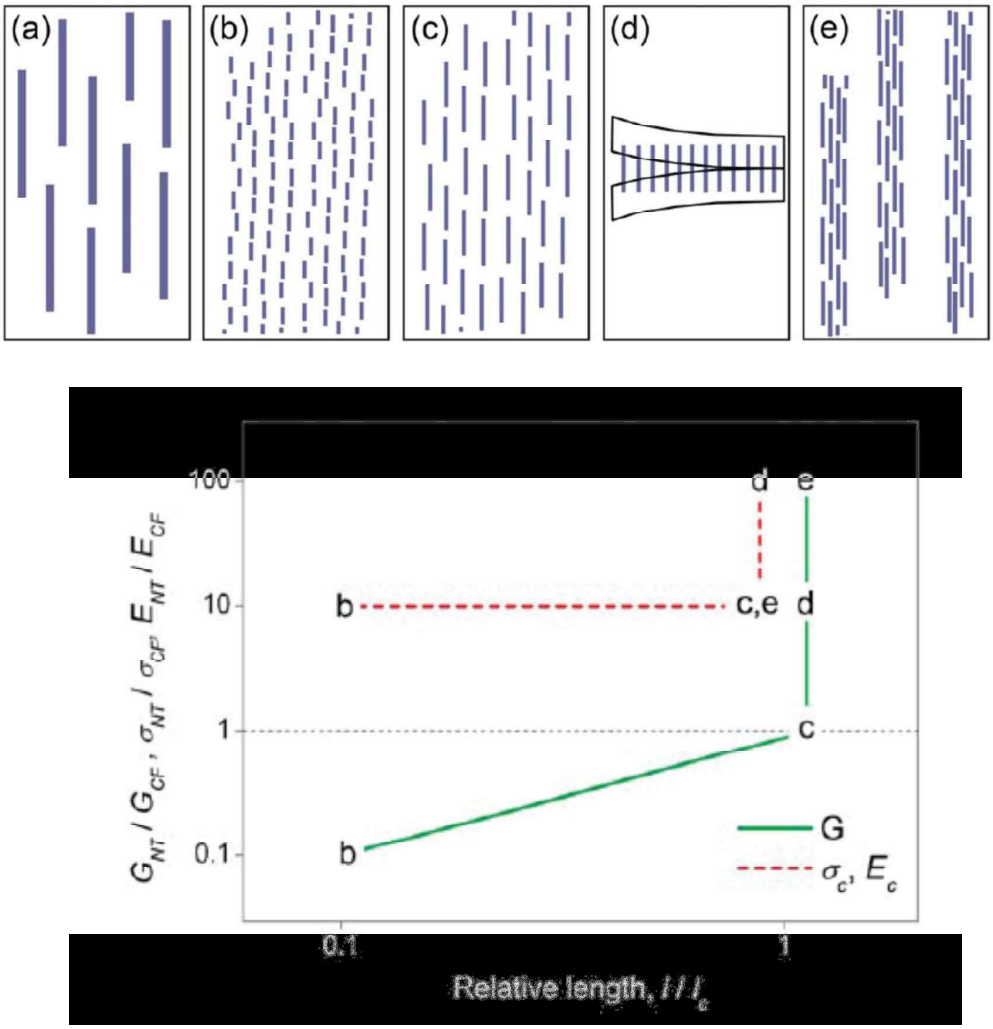

Figure 33. The potential of different nano-reinforcements in terms of relative toughness, strength and stiffness.

Four point bending specimens were fabricated and tested in [56] to determine the ultimate strength and fracture toughness of reinforced composites. The composite specimens were prepared from high-grade commercial alumina with spin-coated interlayers of ductile polymers (PMMA and PVA). In some cases, fracture toughness of the composites was increased by up to an order of magnitude, reminiscent of the natural layered composites (see Figure 34 for example). It was proposed that this increase may be attributed to an interlocking mechanism, often encountered in biological composites. In Ref. [57], the mechanical properties were further improved by tuning the interphase properties. The Evaporation-Driven Self-Assembly (EDSA) procedure was employed to deposit a thin network of multi-wall carbon nanotubes on ceramic surfaces, thereby generating an interphase reinforcing layer in a multiscale laminated ceramic composite. Significant improvement (up to 90%) in both strength and toughness was demonstrated, all by keeping low volume fraction of nanotubes in the composite (below 0.012%).

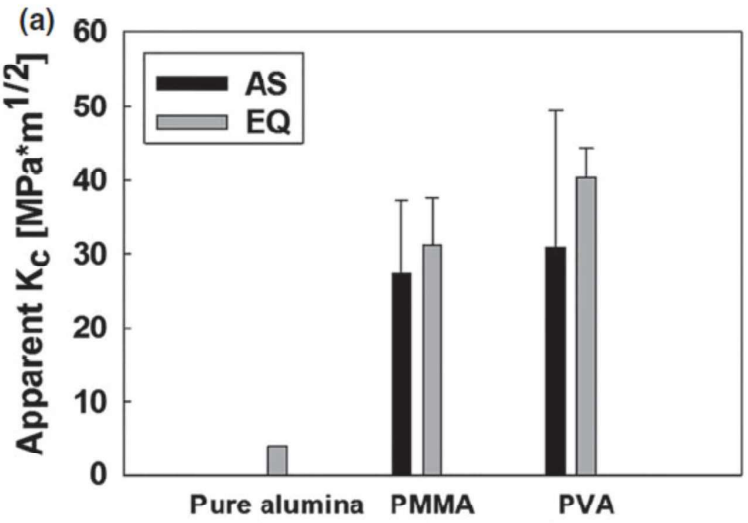

Figure 34. The effect of sample architecture (AS = asymmetric layer arrangement, EQ = equally spaced) and interlayer material on the apparent fracture toughness

4. PROBABILISTIC STUDIES

4.1 Selection of an Acceptable Risk Criterion for Avoiding a Major Fatigue Failure on a Commercial Aircraft (A. Brot, IAI)

Since the accumulation of fatigue damage is a process that entails a large degree of scatter, it is not possible to determine an absolute value of the life to failure. Therefore, a small probability of failure is always present during the aircraft service life. The aircraft manufacturer needs to take every possible step to reduce this probability of failure to an "acceptable value".

There have been several aircraft failures attributed to multi-site damage (MSD) and widespread fatigue damage (WFD) over the last sixty years. The aim of this study is to suggest an acceptable risk criterion that will ensure a very high level of safety for a fleet of commercial aircraft, but will take into account that absolute safety is unattainable. Since most of fatigue related accidents were all related to the MSD and WFD type of failure, the analysis shown is performed on a structure that is susceptible to the MSD and WFD failure mechanism. A damage-tolerance analysis of a typical fuselage lap-splice joint is presented in this paper. This type of structure is prone to MSD which can lead to a WFD catastrophic failure.

A typical fuselage lap-splice joint is analyzed, and inspection intervals are determined using the methodology described in this paper. Figure 35 shows a typical three-row fuselage lap-splice joint where the outer side usually has countersunk fastener heads. The critical location for fatigue is at the countersunk fastener head at the first row.

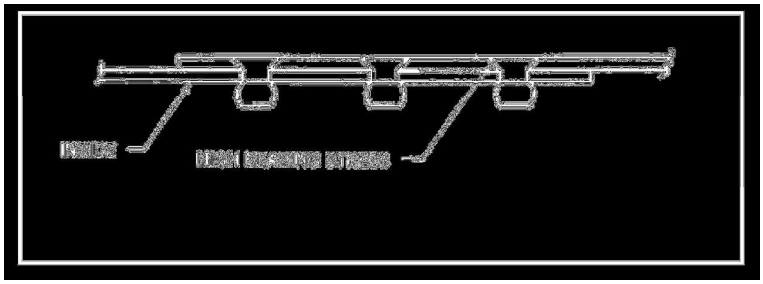

Figure 35. Typical fuselage lap-splice joint

The example chosen is a typical lap-splice for the fuselage of a narrow-body jet airliner (a narrow-body airliner was selected since it usually accumulates many more flight cycles in its service life than a wide-body aircraft). The splice material was taken as 2024-T3 aluminum sheet having a material thickness of 0.050 inches. Aluminum rivets of 0.1875 inch diameter with countersunk heads were taken, installed in three rows with a pitch of 1.0 inch between fasteners. A nominal pressure differential of 8.6 psi at cruise altitude was assumed. The fuselage radius was taken as 74 inches, as being typical for narrow-body jetliners. The aircraft was assumed to have a limit-of-validity (LOV) of 75,000 flights, after which the aircraft must be retired from service.

Several researchers have developed analysis methodology for widespread fatigue damage of a lap-splice using a deterministic analysis; an example is shown in [29]. Several papers on WFD of a lap-joint that use probabilistic software called INSIM were presented [30-32]. It appears that more realistic WFD analyses can be performed using the probabilistic approach. The INSIM (INspection SIMulation) computer program has been developed in order to simulate the entire fatigue environment that a structure must withstand. INSIM simulates, in a probabilistic manner, service life variation, service load severity, time to crack-initiation, crack growth history and NDI detection capability, as is described in [33].

There are three, mutually exclusive, outcomes of the fatigue process:

(1) The component may reach the end of its operational life and be retired from service.

(2) A crack may be detected during scheduled maintenance operations. The affected part is usually repaired or replaced.

(3) A crack reaches its critical size undetected and the structure fails in service.

Crack initiation, crack growth and crack detection characteristics of a specific structural location are input into INSIM, which performs the simulation of the fatigue process for the entire virtual fleet. Cracks initiate at various times and grow at variable rates in each aircraft. Inspections are performed according to a predetermined schedule. Cracks are detected during these inspections according to the statistical expectation of detection. As the simulation proceeds from aircraft to aircraft, cracks are detected, aircraft are retired from service or failures occur. In order to provide statistically significant results, a large number of simulations must be performed. Based on these simulations, INSIM calculates the probability that failure has occurred. Figure 36 shows a typical output summary from an INSIM analysis consisting of one million simulations.

Fleet Size: 1,000,000		Threshold 15,000	Interval(s): 6000
Mean Service Life:	40,006	High-time:	60,618
Min. crack initiation:	607	Max. crack initiation:	50,647
Min. crack growth:	10,391	Max. crack growth:	23,773
Inspections performed:	2,702,731	Inspections per aircraft:	2.70

	Number of Components	Percent
Component retired uncracked:	7957	0.80%
Component retired cracked:	55,292	5.53%
Cracks < Ap detected:	932,958	93.30%
Cracks > Ap detected:	3492	0.3492%
Failures:	301	0.03010%

Figure 36. A typical INSIM output summary

Table 4 presents results from a probabilistic analysis of a lap-joint using INSIM software. From the "design conditions" shown in Table 4, it appears that widespread fatigue damage (WFD) is extremely improbable, since crack initiation and growth will take about 286,000 flights while the maximum service life is only 75,000 flights. When only the spectrum and scatter considerations are accounted for, crack initiation and growth will now take a minimum of 17,150 flights, making failure possible, with the cumulative probability of failure (CPOF) calculated as 0.240%. At this stage, no inspections for cracking have been specified. Adding high-frequency eddy-current (HFEC) inspections at 3,500 flight intervals will reduce the CPOF to only 0.0012%.

Finally, keeping the maximum service life at 75,000 flights, but accounting for a mean service life of 65,000 flights drops the CPOF further to 0.0008%.

	Crack Initiation	Crack Growth	Initiation + Growth	Mean Service Life	Maximum Service Life	Cumulative Probability of Failure
Design Conditions	265,400 Flights	20,670 Flights	286,070 Flights	75,000 Flights	75,000 Flights	–
Spectrum & Scatter Considerations	5,500 Flights (Minimum)	11,650 Flights (Minimum)	17,150 Flights (Minimum)	75,000 Flights	75,000 Flights	0.240%
Inspections at 3,500 Flight Intervals	5,500 Flights (Minimum)	11,650 Flights (Minimum)	17,150 Flights (Minimum)	75,000 Flights	75,000 Flights	0.0012%
Inspections & Early Retirement	5,500 Flights (Minimum)	11,650 Flights (Minimum)	17,150 Flights (Minimum)	65,000 Flights	75,000 Flights	0.0008%

Table 4. A probabilistic analysis of widespread fatigue damage

INSIM was run for a variety of inspection intervals, all using high-frequency eddy-current (HFEC) crack detection methodology. In all cases, the inspection threshold was kept at 14,000 flights. Figure 37 shows the results of this analysis. If we take 0.001% as a tentative acceptable value of CPOF, then an inspection interval of 3500 flights is appropriate. Figure 38 shows typical values of the hazard-rate as a function of the aircraft service life, as was determined by INSIM. It clearly shows the increase in hazard-rate as the aircraft service life is increased. It also demonstrates the peaks and valleys of the hazard-rate parameter, with a peak occurring just before an inspection takes place, and a valley occurring just after the inspection, when cracked aircraft are removed from service. Since the CPOF parameter deals with the overall probability of failure, it does not have the ability to detect specific potentially dangerous situations that occur as an aircraft approaches its limit of validity, when it is required to be retired from service. Therefore, the hazard-rate may be the more appropriate parameter (the hazard-rate is defined as the probability of failure occurring during the next flight). Ref. [34] discusses USAF applications of the hazard-rate, which is called the "single flight probability of failure" in
Ref. [34].

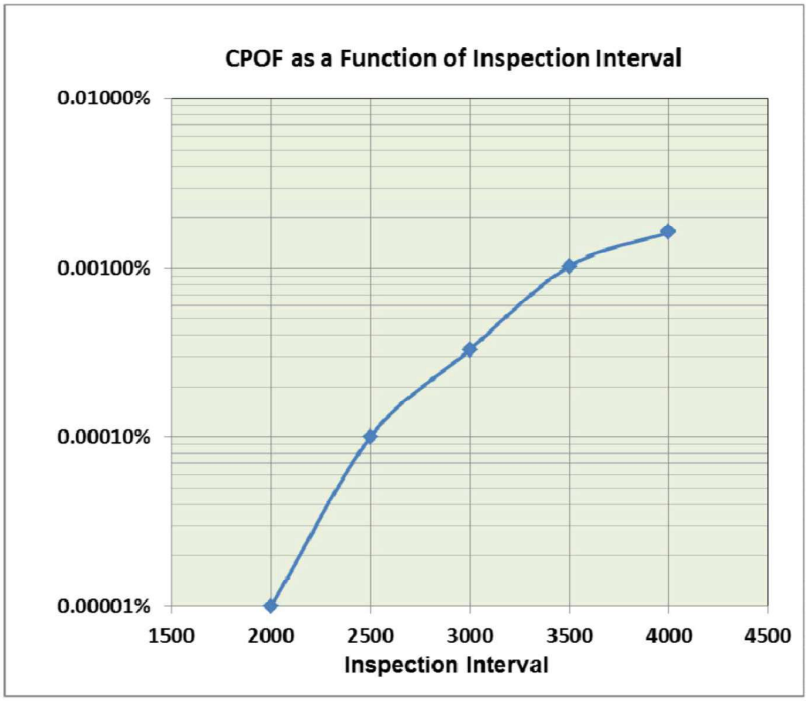

Figure 37. The Cumulative Probability of Failure (CPOF) as a function of the inspection interval

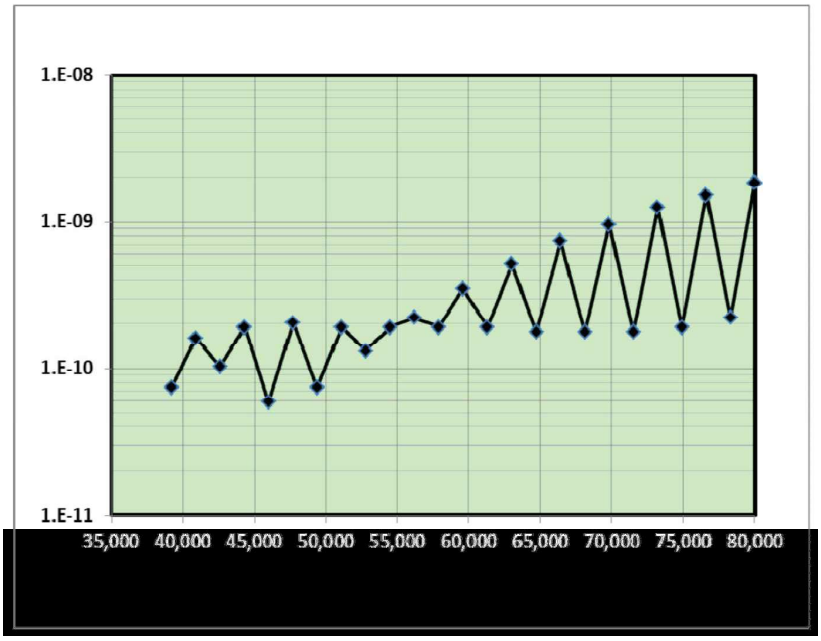

Figure 38. Value of calculated hazard-rate as a function of service life (the hazard-rate is defined as the probability of failure occurring during the next flight)

As was stated previously, several probabilistic models are used in the INSIM software. Table 5 describes the various probabilistic models that are used.

Function to be modeled	Probabilistic Model Used	Comments
Number of flights to crack initiation	Two-parameter Weibull distribution	Accounts for both scatter and spectrum variations
Number of fights of crack growth until failure	Normal distribution accounting for scatter and spectrum variations	Limited to ± 3 standard deviations
Aircraft retirement	Normal distribution around the mean service life. Maximum service life is defined as 3 standard deviations above the mean	Limited to ± 3 standard deviations
Crack detection	Three-parameter Weibull distribution that defines crack detectability	Uses established parameters for various NDI methods

Table 5. Probabilistic models used in INSIM

Table 6 shows typical INSIM results as a function of the number of program simulations that were performed. With only 100,000 simulations, insufficient data is available to accurately predict CPOF. As more simulations are performed, the range of crack initiation broadens (as defined by the Weibull distribution) while the range of crack growth remains nearly constant. At two million or more simulations, the crack growth range reaches the limits shown in Table 5. As a result of these effects, the value of CPOF tends to converge, with more and more simulations, to a value of 0.0011%. Typical INSIM runs are performed with approximately two million simulations, which can be performed on a desktop computer in only a few minutes.

Number of Program Simulations	Cumulative Probability of Failure (CPOF) with an Inspection Interval of 3,500 Flights	Range of Crack Initiation (Flights)	Range of Crack Growth (Flights)
100,000	–	15,230 – 747,800	11,750 – 35,945
200,000	0.0005%	11,430 – 709,600	11,730 – 36,580
500,000	0.0009%	8,690 – 746,400	11,650 – 36,600
1,000,000	0.0009%	9,360 – 779,100	11,560 – 36,880
2,000,000	0.0012%	7,560 – 763,400	11,560 – 37,050*
3,000,000	0.0011%	6,930 – 784,500	11,560 – 37,050*
4,000,000	0.0011%	6,930 – 784,500	11,560 – 37,050*

* Maximum range permitted by INSIM per Table 5.

Table 6. A statistical review of INSIM results

The full length paper (Ref. [35]) describes and develop the WFD analysis of the lap-joint in much more detail, and includes detectability criteria for multiple cracks. Based on the results shown in the probabilistic analysis, criteria for selecting an "acceptable value" of CPOF and hazard-rate to avoid a major fatigue failure are presented.

5. STRUCTURAL HEALTH MONITORING

5.1 Research activities in Ben Gurion University HUMS Laboratory (J. Bortman, BGU)

In recent years, Ben Gurion University (BGU) Health and Usage Monitoring Systems (HUMS) Laboratory, leaded by Prof. Jacob Bortman, focuses on application of vibrations and acoustical measurements for early detection of damages in mechanical components. Vibration monitoring can be used to detect machine faults, including: unbalance, misalignment, oil film bearing instabilities, roller bearing degradation, gear damages, mechanical looseness, structural resonance, and cracked rotors. It is applicable to a range of industrial machines such as energy turbines, engines, helicopters, ships or land vehicles.

Ref. [58] deals with detection and monitoring of failures in bearings using optic fiber sensors that measure the strain and temperature changes. Miniature sensors were placed in specific locations at the bearing house, and the signal to noise ratio of the bearing vibrations was considerably enhanced, while the transmission path issues were reduced. Bearing faults were successfully measured and the promising potential of this method was demonstrated. Series of basic tests were conducted to better understand the influence of the different factors involved when designing the sensor. A similarity of the response was demonstrated for two variables that were tested. An example of the damage identification capabilities is shown in Figure 39.

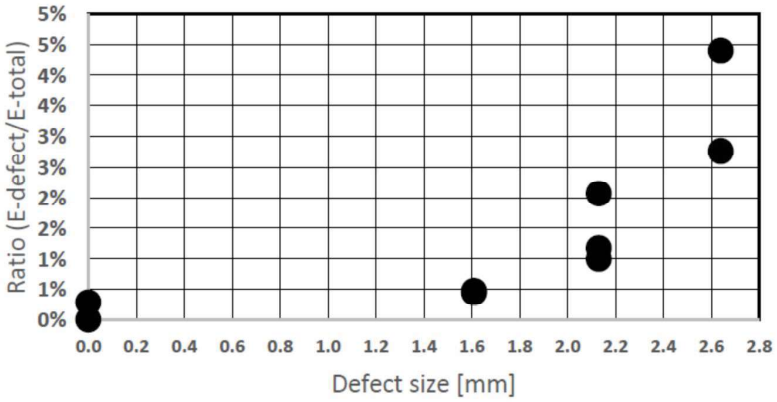

Figure 39. The ratio of E_{defect}/E_{total} versus defect size (measured by fiber optic sensors)

A practical method for the enhancement of systems Reliability, Availability, Maintainability, and Safety (RAMS) assessments was introduced in Ref. [59]. The method is based on conducting correlations between deterioration stages and the remaining useful life of the product. Reliability is continuously updated according to pre-calculated Weibull parameters based on historic deterioration stages accumulated data and concurrent condition management findings. The updated assessment represents the real system condition along its deterioration stages. The method enables improved decision making operation and maintenance action thus

lower the Life Cycle Cost (LCC). The method presented is named "Condition Based-RAMS" (CB-RAMS).

In Ref. [60], vibration monitoring and orbital paths observation were used to detect the presence of a flaw in a shaft. Two types of flaws were tested: a straight slot, and a fatigue crack. For both flaw types, specimens of different depths were examined in order to assess the detection capability. A new approach to examine vibrations at the critical speed was proposed; this speed is chosen because of the strong connection to the basics of the physical problem.

The presence of a straight slot in the shaft was found to be related to a decrease in the natural frequency and to a decrease in amplitude of the first order at critical speed. For the fatigue crack, a consistent trend in critical speed and in amplitude was not seen as crack depth grew. A new method to detect the change in the shaft natural frequency was proposed. The decrease in the shaft's natural frequency was found to be correlated with the flaw depth. The orbital paths created at different rotating speeds allow for flaw detection through changes in shape, amplitude, and phase. The combination of two indicators, change in critical speed and change in amplitude at critical speed, were suggested for classification of flaw size. For the straight slot case, the method proposed was able to distinguish between different fault depths (Figure 40).

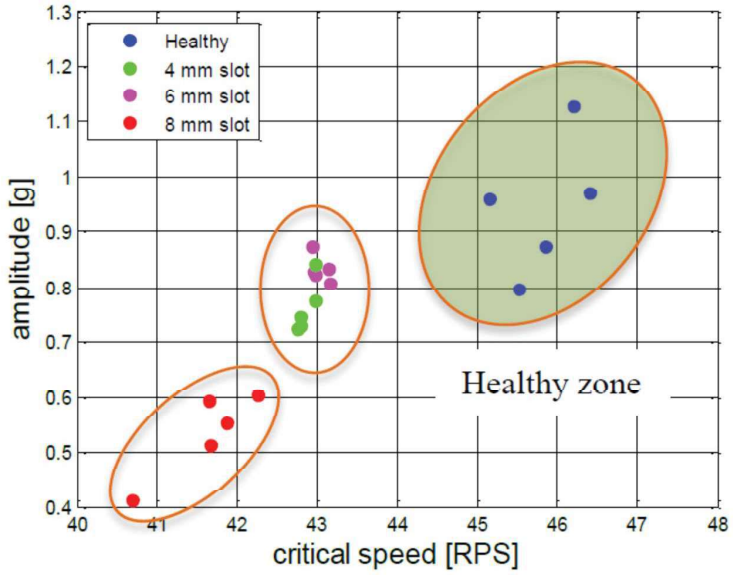

Figure 40. Amplitude versus critical speed for a straight slot flaw type. Three distinct groups of flaws are clearly observed: intact, 4-6 mm and 8 mm.

Finally, Ref. [61] presents two methods for fault prognostics in rotating gears: a modified synchronous average and an adaptive difference. The modified synchronous average is designed to overcome the sensitivity of the regular synchronous average to cumulative phase

errors. The adaptive difference is a signal derived from the synchronous average and it is designed to separate effects of local faults in one tooth of the gear from the dominating effects of distributed faults. The algorithms' efficacies were examined and demonstrated on simulated signals generated using a dynamic model.

5.2 Optical Fibers Based Cure Monitoring for Boeing 737 Fuselage Skin Composite Repair (I. Kressel, IAI)

The concept of using bonded composite patches for the repair of aging metallic aircraft has proven to be both a preventive measure, as well as a method for delaying future growth of existing damage [87]. The main advantages of a bonded patch repair, as compared to a metallic bolted one, are: smoother load transfer, good fatigue and damage-tolerance behavior of the composite patch, and ease of application on curved surfaces.

Bonded composite repair concept uses composite fiber plies, which are cured and bonded directly on the damaged structure, under vacuum at elevated temperature. The structural performance and long life durability of the repair critically depend on good surface preparation of the metallic substrate and close control of the temperature profile, over the entire patch area, during the whole curing process. These are also required by the airworthiness requirements for Transport Category Airplanes [94], specifically requirements 25.307 and 25.603 and relevant guidance. Despite its superior structural performance in restoring both static and fatigue strength over the conventional bolted repair, this bonded composite repair concept has not been widely adopted as a standard repair for commercial aircrafts. This may be partially due to the absence of direct assessment of the structural integrity of the repair during application and service. Currently, the standard bonding and curing process monitoring is performed mainly by tracking the temperature around the bonded patch, using electrical thermocouples. While the quality of the repair can be assessed in terms of the absence of debonding, delaminations and cracks, using ultrasonic and eddy current techniques, no clear indication may be obtained regarding the degree and quality of the structural bonding between the patch and the metallic substrate.

The introduction of the smart repair concept [88, 89] is aimed towards real-time monitoring of both the curing process and the repaired structural integrity over time. Embedded fiber-optic sensors have the potential to not only monitor the curing process but also to continuously check for a possible deterioration of the repair airworthiness, thereby reducing maintenance cost by satisfying regulatory requirements for replacing conservative scheduled maintenance with condition-based maintenance.

Quite few successful attempts have been made to use fiber Bragg grating (FBG) sensors for direct tracking of strain development during curing of composite materials [90]. The residual strains, induced by the change in the chemical reaction of the composite materials matrix were measured [91] with good correlation to the degree of cure. It was also demonstrated that the embedded fibers do not cause any significant degradation in the structural performance of the structure.

In this study, a Carbon-fiber co-cured patch repair was applied on a Boeing 737 fuselage dent located forward of STA 360 splice, near stringer 26, as seen in Figure 41. The dent size was 50 mm by 30 mm, with a maximum depth of 5 mm. This dent exceeded the Boeing Standard Repair Manual limitation and therefore no fasteners based repair was a viable option within the acceptable aircraft down-time. The skin material is 2024-T3, 0.071" thick, with chemical milling up to 0.063" at the dent location (measured). The installation of the bonded repair was substantiated by stress analysis based on the FAA Policy document on bonded repair size limits (PS-AIR-20-130-01), that states the following requirements:

- The original structure should sustain Limit loads without taking credit for the bonded repair
- Demonstrate Ultimate Load carrying capabilities, taking credit for the repair.

While not enough data has been collected for approval of this method as satisfactory proof of compliance with airworthiness requirements for commercially operated transport category aircraft [94], it was approved by CAAI for application on an aircraft holding an "Experimental" certificate of airworthiness.

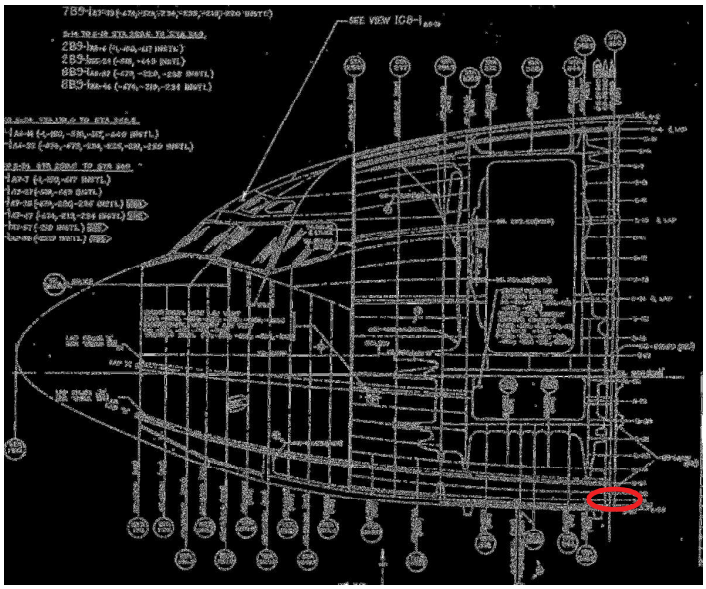

Figure 41. Dent location

Four optical fibers, evenly spaced, each with three FBG sensors, were placed directly over the 200×200 mm patch during its application. One sensor in each fiber was placed outside the patch so that it was only affected by the temperature. Typical time history readings of the Bragg sensors during the cure process can be seen in Figure 42. It is clearly seen that the two sensors (FBG-1 and FBG-2) placed on the patch, experienced significant residual strain readings after the cure cycle ended, and the temperature had stabilized to room temperature. As expected, the free sensor located outside the patch (FBG-3) returned to its room temperature value as the cure cycle ended.

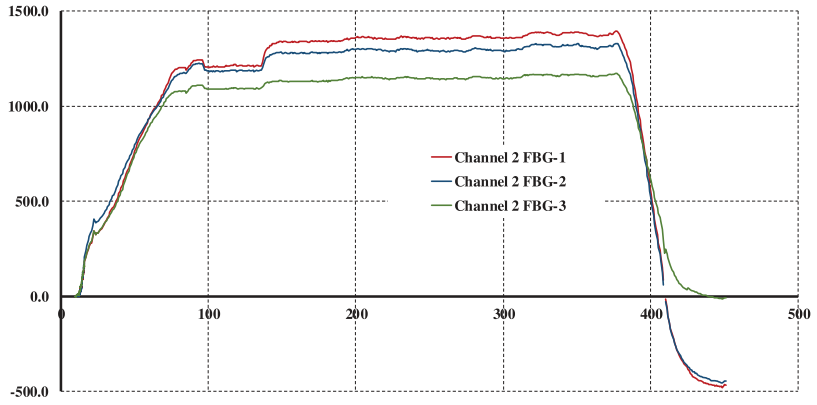

Figure 42. Typical readings of Bragg sensors during the cure process

The optical strains ($\Delta\lambda/\lambda$), as measured by both the embedded and free FBGs during curing, can be used to calculate the equivalent thermal expansion coefficient. Plotting the embedded FBGs vs. temperature (as measured by the free FBG, Figure 43) reveals a significant difference between the heating and the cooling phase. It is clearly seen that during the heating phase, the equivalent thermal expansion coefficient is relatively low, indicating that the patch is floating on the metal substrate with no structural bonding. During the cooling phase of the cure cycle the equivalent thermal expansion coefficient is dictated by the metal substrate, indicating that a structural bonding has been achieved.

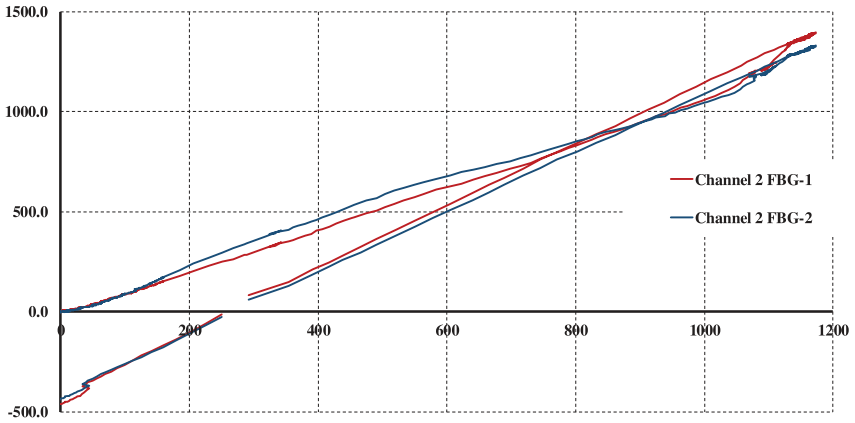

Figure 43. Typical readings of Bragg sensors: embedded FBGs vs. free FBG

This work introduces a practical structural assessment concept for bonded repairs, using embedded fiber optic FBG sensors. This technique allows bond tracking by following the development of mechanical strains in the patch during curing, induced by the large difference in the thermal expansion coefficient between the composite patch and the metal substrate. It is

expected that in-service data collection and analysis will allow substantiation of the proposed repair monitoring method for commercially operated aircraft, resulting in reduction of aircraft down time and maintenance costs.

6 MISCELLANEOUS

6.1 ICAF 2017 Plantema Memorial Lecture - Three Faces of Aeronautical Fatigue (Abe Brot)

The following abstract summarizes the Plantema lecture given in ICAF 2017 by Abe Brot [62].

- **Face 1: We had Eyes but Could Not See**

During 1969, an incident occurred at a large aircraft engine company. The company received many orders for a specific aircraft engine model. The demand for these engines was so high, that the company employed subcontractors to manufacture several of the complex engine parts, in parallel with "in-house" manufacturing. Soon after the engines entered service, several airlines reported fatigue cracks and failures of the "high-compressor duct". Analysis of these failures disclosed that nearly all of the fatigue failures occurred on ducts manufactured by the subcontractor.

The first step of the investigation was to compare several ducts produced by the subcontractor and those produced in-house, against the design and manufacturing specifications. It was found that all the ducts produced in-house, and all those produced by the subcontractor met all the design and manufacturing requirements.

Engine testing was performed, installing ducts produced by the subcontractor. When the high-rotor reached about 6,800 RPM, the pressure-transducers began "shrieking" at 1350 Hz, while the strain-gages and accelerometers were "dancing" at the same frequency. The peak measured noise levels reached 170 dB while the measured stress levels on the duct were 18 to 20 ksi, which certainly could explain the high-cycle fatigue failures. As the high-rotor speed reached 8,800 RPM, all the measured parameters suddenly quieted down. Engine testing with in-house produced ducts, did not show any of these characteristics.

Subsequent testing showed that the source of the noise and vibration was an acoustic resonator that was present in a chamber of the engine. There still were no indications why only the ducts produced by the subcontractor were affected. Eventually, the mystery was solved, but more than sixty high-compressor ducts failed in service. This problem took about eight months to solve, at a very high cost to the company.

- **Face 2: Nearly Identical Twins or Distant Cousins?**

Over the last half-century, organizations that dealt with fatigue life variability of aircraft structures, generally performed their reliability analyses by using the Weibull distribution. The Log-Normal distribution was considered to be nearly identical to the Weibull distribution, and it was less often utilized.

It has been shown in this paper, using several actual examples, that there are very sizable differences between the Weibull and Log-Normal distributions, for setting allowable service lives to minimize the probability of failure. In all cases, the Weibull results are much more

conservative than the Log-Normal results. From these results, it is difficult to say which distribution is the more accurate.

An analysis was performed to determine the allowable service life of a steel landing gear. The results clearly indicate that the Log-Normal distribution predicts a much lower probability of failure during its service life than the Weibull distribution.

In 1969 and in 1972, the Boeing Company published the results of a detailed study that was performed on fatigue life variability of aluminum, titanium and steel aircraft structures. Boeing concluded that the Log-Normal model produced an optimistic assessment of the fatigue data distribution, while the Weibull model produced an acceptable assessment of the fatigue data distribution. The author of this paper found it difficult to accept the above conclusions without further investigation, due to the manner that the test specimens were selected.

A sixty-specimen fatigue test program is proposed in the paper in order to better evaluate the fit of the Weibull and Log-Normal distributions to actual fatigue test data.

- **Face 3: Widespread Fatigue Damage Revisited**

During October, 2011, The FAA released AC No. 120-104, which is an advisory circular dealing with "Establishing and Implementing Limits-of-Validity to Prevent Widespread Fatigue Damage". In this document, the FAA suggested that the manufacturer perform sufficient fatigue testing and analysis, under typical spectrum loading, to determine the service life at which 50% of the fleet has already failed. This service life is called $WFD_{average}$ in this advisory circular. The advisory circular then suggests that 50% of the $WFD_{average}$ be identified as the "Structural Modification Point" (SMP), at which the manufacturer is to implement structural improvements to the structure, in order to ensure that widespread fatigue damage will not occur. This implies that if the manufacturer elects not to implement any structural improvements, 50% of $WFD_{average}$ will become the limit-of-validity (LOV) of the aircraft.

This does not seem to be a reasonable suggestion to ensure safety, for two reasons:

- Since $WFD_{average}$ is primarily based on the crack-initiation life of the structure, it is basically a return to the "safe-life concept", which has been shown many years ago to be an unreliable method to ensure safety of fatigue critical structures.

- Setting the LOV at 50% of the "safe life" is certainly insufficient. Scatter-factors of 5 or more are normally used to provide sufficient safety of safe-life structures.

An alternate approach is presented in this paper to define the LOV of the suspected structure:

Determine the appropriate allowable hazard-rate for the structure. AC No. 25.571-1D and other FAA documents imply that a hazard-rate of 10-9 failures per flight hour will result in sufficient safety (hazard-rate is defined as the probability that the "next flight of the aircraft" will result in a catastrophic failure.)

Perform probabilistic analyses using INSIM Software to determine the inspection thresholds and intervals that are appropriate for the selected LOV for the "AC No. 120-104" approach as well as the "alternate" approach. The results of these probabilistic analyses will predict the maximum hazard- rate before the LOV is reached. In this way, the results of using the methodology suggested in AC No. 120-104 will be compared to those using the alternate approach described above.

The Plantema paper develops these topics and compares the results of the probabilistic calculations, using both approaches. A selected example of a typical narrow body aircraft is used for the analysis. Discussion and conclusions are included in the paper [62].

6.2 Research activities in Ben Gurion University Computational Mechanics Laboratory (Z. Yosibash, BGU)

In Ref. [63], the energy release rate (ERR) proposed by Irwin based on a theory by Griffith has been extensively used as a fracture criterion in 2D for brittle domains. Under in-plane mixed mode loading (modes I+II), the direction of crack initiation from cracks and sharp V-notches was determined by the orientation at which the ERR attains its maximum. Using a newly developed asymptotic expansion verified by direct results from finite element analyses we demonstrate that the ERR under mode III cannot predict the fracture initiation direction correctly. The ERR maximum value is always obtained along the V-notch bisector, contrary to experimental observations. This forbids the ERR to be applied as a failure initiation criterion in cases where mode III is dominant.

In Ref. [64] a three-dimensional failure initiation criterion in brittle materials containing a sharp V-notch is presented and validated by experiments. It is based on simultaneous fulfillment of the stress requirement and a finite fracture mechanics energy release rate (ERR) requirement.

Since the ERR cannot determine failure initiation direction for dominant mode III loading, the failure initiation orientation is determined solely by stress considerations and the force at fracture is determined by both ERR and stress requirements. Experiments on PMMA, Graphite and MACOR V-notched specimens loaded by three modes demonstrated that predicted fracture load was mostly within 6.5% (RMS) of experimental values.

In Refs. [65-66] we addressed theoretical topics in the field of fracture mechanics as the T-stress and failure criteria in the vicinity of sharp V-notches under mode I and mode II loading.

6.3 Research activities in Tel Aviv University Dreszer Fracture Mechanics Laboratory (L. Banks-Sills, TAU)

During 2015 and 2016, a continuation of our interest has been in the effect of reinforcement of a polymer with low weight fractions of carbon nanotubes (CNTs). The influence of CNT concentration on the fracture toughness of poly(methyl methacrylate) (PMMA) was examined on single-edge V-notched-beam (SEVNB) specimens [67]. Six groups of SEVNB specimens containing 0.5, 1, 2, 4, 8.5 wt% of CNTs and neat PMMA as a reference were tested. First, a notch was introduced into the specimens by a specially made disk whose edge is V-shaped with a 30° angle and a 30 μm tip width. As suggested by an American Society for Testing and Materials Standard for polymers, induction of a natural crack was attempted, without success. Therefore, fracture toughness values were determined with the sharp machined notch by means of a K-calibration formula. These were compared to values obtained using a stress concentration factor and found to differ by less than 3%. The latter calculation took into account the geometry of the notch. Results showed a decrease in the fracture toughness values with an increase in the CNT concentration. For specimens in which a natural crack was attempted, a significant increase in the apparent fracture toughness was observed, as a result of the induced damage. A presentation was made on this subject at the European Structural Integrity Society (ESIS) Technical Committee (TC) 4 meeting [68].

Guy Shiber completed an M.Sc. degree on the characterization of mechanical properties of poly methyl methacrylate (PMMA) reinforced with functionalized CNTs [69]. Functionalization is a process in which the outer surface of the CNTs are treated so that the bonding between them and the polymer is improved. It is thought that this will lead to improved mechanical properties. As a result, of these studies, a paper was published on this subject [70]. The main challenges in successfully using CNTs as a reinforcement phase in a composite are homogenous dispersion and distribution of the CNTs in the matrix, as well as improving the interfacial bond between them. Functionalization of CNTs has proved an effective method for overcoming these challenges. The goal of this study was to determine the mechanical properties of a composite material using experimental methods. The PMMA matrix was enhanced by different weight fractions (wt%) of nanotubes functionalized by two methods. Carboxylated CNTs were further functionalized by the grafting from (GF) and the grafting to (GT) methods. The effect of these functionalization methods on the CNTs was evaluated through measurement of effective mechanical properties of a composite containing them, as well as, through a comparison to a previous investigation, in which non-functionalized (NF) CNTs were employed. Tensile tests were carried out on neat PMMA and PMMA containing functionalized CNTS; there were two GF batches containing 0.8 wt% and 1.5 wt% of CNTs; and three GT batches containing 1.5 wt%, 3 wt% and 6 wt% of CNTs. It was seen that the addition of a weight percent higher than 3 of CNTs to a PMMA matrix increases the elastic modulus of the composite. It was shown that functionalization of the CNTs prior to their introduction into the matrix decreases the weight percent of CNTs needed to produce the same increase in the elastic modulus for non-functionalized CNTs. Low CNT content, both functionalized and non-functionalized, may cause a decrease in the elastic modulus or produce a similar value as that of the matrix.

In addition, another area of interest is that of the characterization of the behavior of delaminations between plies of fiber reinforced, laminate composite material. A review paper was published on this subject [71] and several lectures were given summarizing these results [72-74]. A methodology for measuring the interface fracture toughness of a crack between two isotropic, homogeneous materials and a delamination between two laminate of unidirectional composite materials of differing directions was presented. Four cases were considered. Two isotropic material pairs were described: glass/epoxy and two ceramic clays. Similar studies were presented for two cross-ply laminates: 0°/90° and +45°/- 45°. The double slash indicates the location of the delamination. The Brazilian disk specimen was used to carry out mixed mode fracture tests. For the isotropic material pairs, the specimens are illustrated in Figure 44. The cross-ply specimens are shown in Figure 45. The load and crack or delamination length at fracture were measured and used in a finite element analysis to determine the displacement field. An interaction energy or M-integral was used to determine the stress intensity factors at failure. These in turn were employed to obtain the critical interface energy release rate G_{ic} and one phase angle ϕ in two dimensions or two phase angles ϕ and ϕ in three dimensions which measure the mode mixity. For the M-integral and for each interface crack or delamination, the first term of the asymptotic solution of the field quantities is required. For two isotropic materials, these solutions are well known. For the laminates described here, they were determined by the Stroh and Lekhnitskii formalisms. A failure criterion determined from first principles was presented. The values of G_{ic} and ϕ in two dimensions or ϕ and ϕ in three dimensions are used to specify the criterion for each material pair. A statistical analysis was presented. Two approaches were taken; one uses the t-statistic to predict a 10% probability of failure; the second uses a standard normal variate to predict a 10% failure probability with 95% confidence.

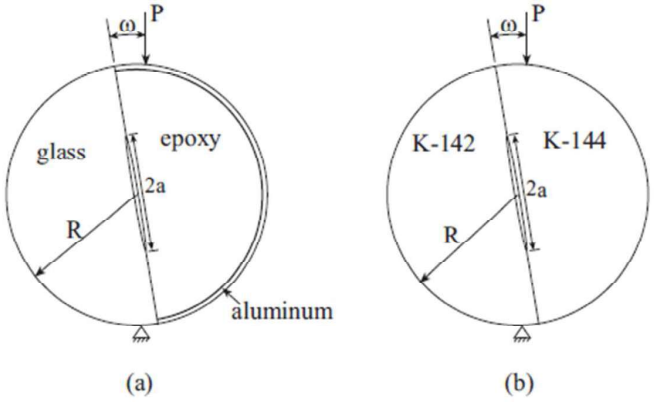

Figure 44. Brazilian disk specimen composed of (a) glass and epoxy and (b) two ceramic clays.

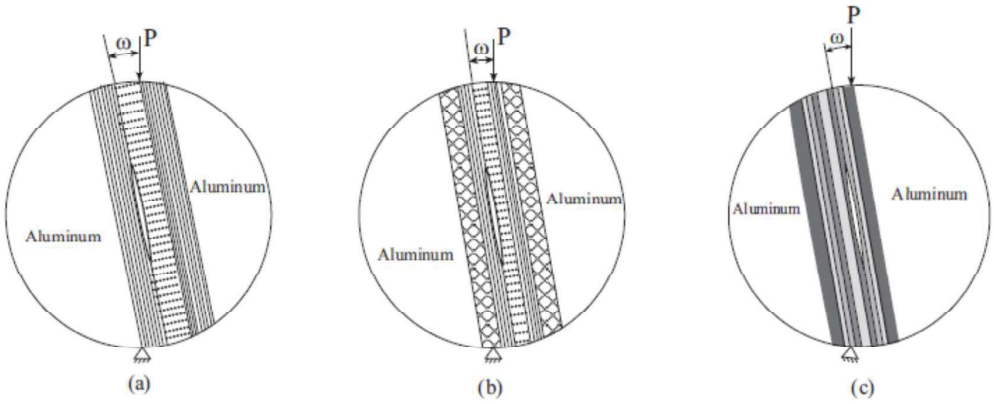

Figure 45. Brazilian disk specimens. Composite specimens containing (a) [0°/90°/0°] strip, (b) [0°/90°/0°] strip with ±45° outer stiffening layers and (c) $[0/-45/+45-0]_s$ strip with ±45° outer stiffening layers.

As an example, for the $+45^\circ//-45^\circ$ interface, a failure surface is shown in Figure 46a, where G_{1c} is the average of normalized interface fracture toughness determined from all tests, and ϕ and ϕ represent different mode mixity combinations. The data obtained in tests presented in [75] are shown as black dots. If one has a structure made of the same materials with such an interface, one may use the failure surface to predict failure. The interface energy release rate and phase angles are calculated for the delamination in the structure. If the points fall below the curve, the delamination is predicted not to propagate. Unfortunately, about half of the test data is below the surface. Hence, a statistical analysis was presented in [71]. The surface shown in Figure 46b is for a 10% probability of failure. For a point calculated from a structure, there is only a 10% chance that the point will fall below the surface and still be critical.

Another student completed an M.Sc. thesis on delamination propagation in a DCB specimen composed of a plain weave multi-directional laminate composite subjected to different cyclic displacement ratios [76]. The composite was made of a carbon/epoxy composite prepreg G0814/913. A double cantilever beam (DCB) specimen was used for the tests as shown in Figure 47. The specimen was comprised of 15 layers alternating between a 0°/90° weave and a +45°/-45° weave. Two papers were published in conference proceedings [77, 78]. A presentation was made at a conference [79] and a paper was published [80].

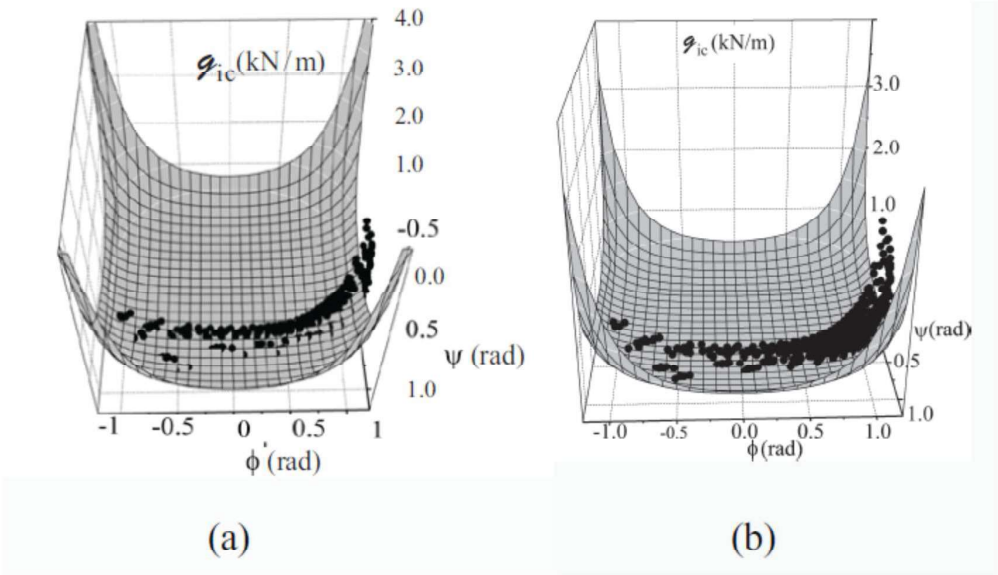

Figure 46. (a) Deterministic failure surface and test points for the +45°/-45° delamination of the graphite/epocy AS4/3502 laminate. (b) Ten percent (10%) failure surface obtained with the t-statistic and test points for the +45°/-45° delamination of the graphite/epoxy AS4/3502 laminate.

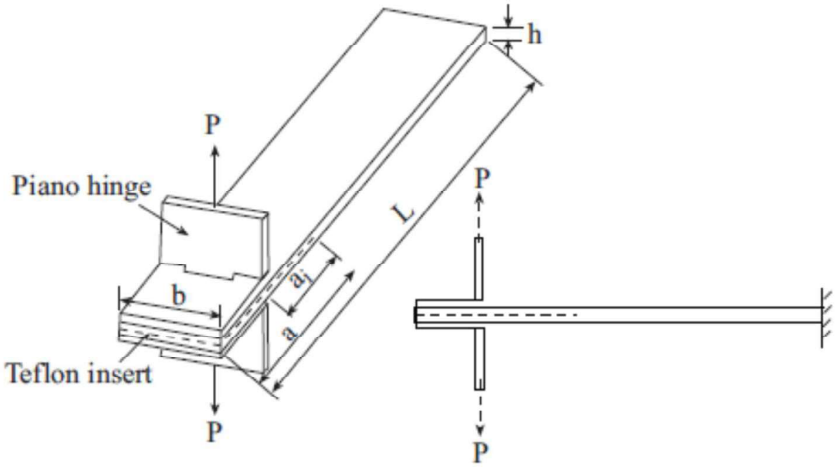

Figure 47. Double cantilever beam woven composite specimen.

A method was proposed for evaluating the delamination growth rate da/dN for any given R-ratio (load or displacement ratio) using data from a relatively small number of tests. First, quasi-static tests were carried out to obtain the resistance GIR-curve. Then, constant amplitude fatigue tests were performed to determine the delamination growth rate da/dN. In both tests, displacement control was imposed. Four different cyclic displacement ratios R_δ,

namely 0.1, 0.33, 0.5 and 0.75, were used for the fatigue tests. When the delamination growth rate da/dN, calculated from the experimental data, was plotted with respect to G_{Imax} and $\Delta G_{Ieff} = (\sqrt{G_{Imax}} - \sqrt{G_{Imin}})^2$, different behavior of the da/dN curves was observed. In addition, modification of the Hartman-Schijve representation was made. When the da/dN data was plotted with respect to the new modified representation which was denoted here as ΔKI , all of the data obtained for different displacement ratios collapsed into one master curve as shown in Figure 48. From this master curve, da/dN values may be calculated for any given R-ratio.

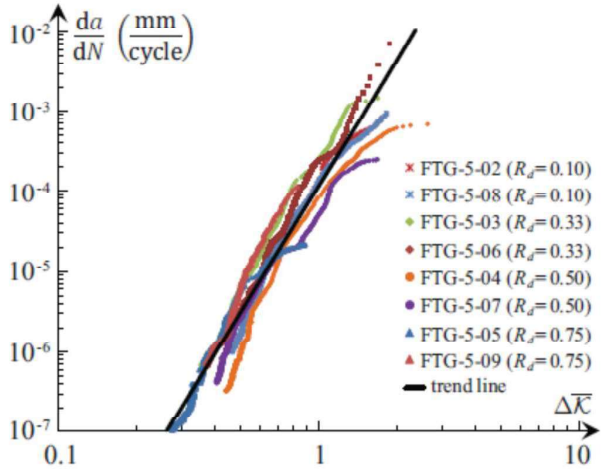

Figure 48. The delamination growth values da/dN plotted with respect to ΔK and the resulting master curve. .

Next, the Virtual Crack Closure Technique for interface cracks was reassessed. An M.Sc. thesis was written on this subject [81]. This method was first presented in 1977 for cracks in linear elastic, homogeneous and isotropic material. It makes use of the Irwin crack closure integral to obtain values of the modes I, II and III energy release rates from finite element data. It may easily be extended to anisotropic material. In addition, it was extended to cracks along an interface between two dissimilar linear elastic, homogeneous and isotropic materials. In that case, the energy release rates were seen to depend upon the size of the virtual crack extension usually taken as the size of the element adjacent to the crack tip. Some attempts have been made to remove this dependence. Nevertheless, in most cases, the accuracy of both the energy release rates and stress intensity factors was not consistently good. In [82], the dependence of the energy release rates on the size of the virtual crack extension for interface cracks was analytically accounted for so that the stress intensity factors may be accurately obtained when fine finite element meshes are used, together with a virtual crack extension consisting of more than one element. A short paper was written and a presentation made on this subject [83]. This method was extended to a specific pair of transversely isotropic materials. It is now being extended to three dimensions to examine if it is possible to obtain accurate results with this method.

Finally, we participated in an ESIS, TC 4, Round Robin. We carried out five fatigue delamination propagation tests on AS4/8552 carbon/epoxy unidirectional (UD) composite DCB specimens with an R_δ-ratio of 0.1. The results were consistent [84]. The Round Robin is leading to an ISO standard for such tests.

6.4 Progress Report at the Mechanics of Composite Materials Lab (R. Haj-Ali, TAU)

The overall goal of the Mechanics of Composite Materials (MCM) Lab at Tel-Aviv University (TAU) is to conduct analytical-computational and experimental scientific research in the nonlinear, multi-scale, and damage modeling of composite materials and structures, micromechanics, computational mechanics, bio-materials, biomechanics of aortic valves, and multi-physics modeling. Over the last two years, the MCM Lab has been engaged in different research projects in the general area of mechanics of composite materials and structures. Two examples are listed below:

1) Integrated microplane model with the HFGMC micromechanics for nonlinear analysis of composite materials with evolving damage [85]

   A nonlinear formulation of the parametric high fidelity generalized method of cells (HFGMC) is offered for the micromechanical analysis of (2D) and (3D) multiphase periodic composites with evolving matrix damage. To that end, the microplane constitutive modeling theory is integrated within the HFGMC to represent the nonlinear and strain softening of the matrix subcells, Figure 49(a). The micromechanical formulation of both the HFGMC and the microplane theories are both developed and integrated. The formulation of the parametric HFGMC, with independent geometrical mapping, is expanded and shown to be well suited for efficient nonlinear computational micromechanics. A new average virtual work integral form is proposed for the HFGMC method which allows for the definition of a generalized internal resisting force vector along with its corresponding stiffness matrix. Unlike the nodal displacement-based finite element (FE), the proposed HFGMC and its weak form are cast in terms of the work-conjugate average displacement and traction vectors, defined on the surfaces (faces) of the subcells. This allows direct interface continuity relations between the hexahedral subcells, , Figure 49(a). The microplane theory is formulated kinematically using its transformed strain with a double split, namely the volumetric (V) and a deviatoric-tangential (DT) splits. The microplane model is implemented with simple 1D continuum damage laws and strain softening, which are used in the two split parts. An application for hexagonal-array of doubly periodic composite, , Figure 49(b), with evolving matrix damage is presented , Figure 49(c).

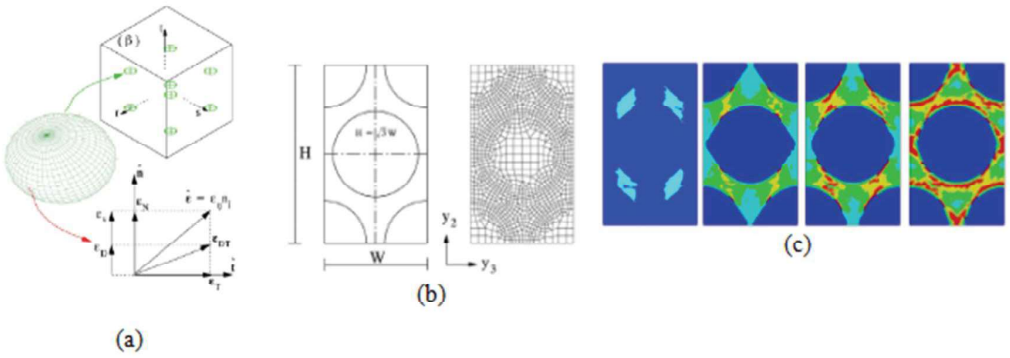

Figure 49. (a) A 3D-parametric HFGMC subcell within a repeating unit cell (RUC) along with integrated micro-plane nonlinear-damage strain paths; (b) An RUC for hexagonal array of unidirectional fibers for unidirectional composite; (c)) predicted failure evolution for an applied transverse stress on the composite.

2) Failure envelopes for laminated composites by the parametric HFGMC micromechanical framework [86]

Micromechanically doubly periodic parametric High Fidelity Generalized Method of Cells, in conjunctions with continuum damage mechanics considerations, is applied to determine failure envelopes of unidirectional composite materials. The methods is based on an incremental procedure in which the local damage variables and global stresses are monitored during the strain softening to provide the value of the envelopes at which ultimate failure occurs. Figure 50(a) illustrates a simple unit-cell used for the parametric HFGMC analysis. The micromechanically established failure envelopes, e.g. Figure 50(b) and (c), are compared with the well-known macro-level based failure surfaces and with experimental data of multiaxial failure stresses found in the literature. It is shown that the new micromechanical failure envelopes are effective in predicting the multi-axis stress failures.

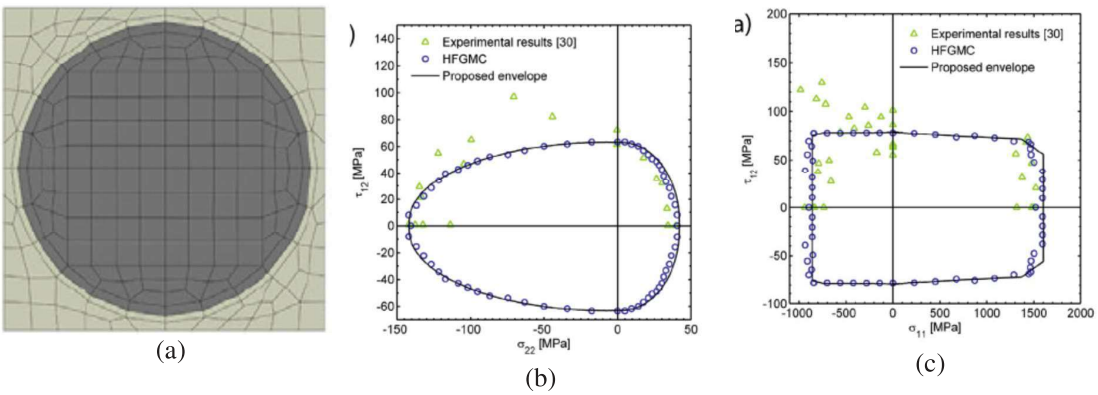

Figure 50. (a) Refined 3D parametric HFGMC repeating unit cells (RUCs) for unidirectional composite with 325 subcells; (b) predicted failure envelope in the transverse stress and axial-shear stress space; (c) predicted failure envelope in the axial stress and axial-shear stress space.

6.5 TaxiBot - A New Concept for Towing Airplanes with Engines Stopped (R. Braier, IAI)

Since the start of the widespread use of towbarless towing, there have been many attempts to tow aircraft directly from the gate to the takeoff runway (dispatch /operational towing) with Engines Stopped, this in order to save fuel and reduce noxious gases and noise pollution. In the past, these proposals have all been dismissed by the airframe manufacturers due to the expected reduction of the fatigue life of the Nose Landing Gear, due to the many towing load cycles that will be applied during dispatch towing.

Nevertheless, the dispatch towing concept has many advantages. A study has shown that an annual savings of $5.3 billion of fuel expenses and 20 million tons of CO2 emission can be realized, if all Wide-Body and Narrow-Body aircraft are towed to their takeoff points (a large 4 engines wide-body aircraft burns about 355 gallons of fuel for every 17 minutes of taxi-out time needed to reach its takeoff point).

IAI, together with TLD and other subcontractors with the support and Airbus and Boeing, has developed a semi-robotic towbarless towing vehicle called TaxiBot (Taxiing Robot). Under this concept, the pilot of the aircraft remains in full command during the entire towing process (called "Taxiboting"), in contrast with the regular dispatch towing where the driver is in control. In order to slow down and /or stop, the pilot is applying the aircraft brakes (at the Main Landing Gears) as needed, as opposed to regular dispatch towing where the tractor is stopping the convoy. By slowing / stopping the convoy by the airplane, the magnitude of the load applied on the Nose Gear is reduced significantly, by the airplane-to-tug mass ratio (10 for wide-body airplanes and 3-5 for narrow-body). This mass ratio and the fact that the bigger mass is stopped by the aircraft brakes is reducing 66%-90% of the physical loads applied to the Nose Landing Gear during the convoy slowdown and braking. The airplane engines will be started-up only shortly before takeoff.

This concept has been proved during a TaxiBot Demonstrator testing, see Figure 51. Test measurements have confirmed that TaxiBot towing will not result in any reduction of the Nose Landing Gear fatigue life.

Figure 51. Airbus A340-600 and Boeing B747-400 towed by TaxiBot

The next step was to build a Prototype to tow Narrow Body (NB) airplanes, to integrate, test and certify. The French company TLD, the biggest GSE manufacturer, produced the TaxiBot NB prototype basic vehicle which was tested these during one and a half years in Chateauroux airfield in France.

The program acquired a grounded A320-200 airplane and instrumented it to serve as real condition test bed, see Figure 52. At June 2013 the first pre-serial production TaxiBot NB the PRS1 was delivered to Frankfurt airport for adaptation and testing with a B737-500 test airplane, provided by Lufthansa. Till the end of March 2014 the following PRS2 and PRS3 were delivered to Frankfurt to support the certification tests campaign.

Figure 52. TaxiBot NB prototype towing the Airbus A320-200

The B737-500 is the most challenging platform in the Narrow Body commercial aircraft manufactured by Boeing and Airbus, since the mass ration between the aircraft and the vehicle is ~2 (A/C MTOW 54 tons and vehicle weight 26.5tons). In addition, the loads on the NLG of this airplane are the highest in the B737 family and the A/C wheel base is the shortest in the family. The lowest mass ratio, the shortest wheel base and the highest NLG loads on the
B737-500 are the most extreme case and the most challenging for the TaxiBot control system in terms of controlling the loads on NLG, since the weight of the vehicle comparing to the A/C weight is about 50%. The short wheel base is also the most challenging case from the steering stand point; since the A/C maneuverability is greater than all other airplanes (A/C maneuverability is greater as much as the wheel base is smaller). High maneuverability generates high sensitivity to pilots steering inputs, which become over sensitive above 15knots. We had to develop a special algorithm to adapt the TaxiBot reaction to pilot steering inputs in order to give the pilot a "transparent feeling" at all speed ranges from 1 knots to 22-23 knots.

Following the final adaptation for the B737-500 the certification test have started in Frankfurt with EASA and CAAI certification authorities. The certification test included 132 test of all emergency cases and malfunction on the system as well as careful testing and measurements of the TaxiBot ability to maintain the designed fatigue envelop defined by IAI experts with the support of Boeing. Keeping the fatigue envelop in real time under all normal taxiing

condition and the static envelop in all emergency cases were the main focus of the authorities, that participated and witnessed the testing, via a real time display of the loads measured during the tests. Finally in October 2014 the TaxiBot have granted the Supplement Type Certificate (STC) for the B737 classic family. Following the certification document issued by EASA the TaxiBot PRS vehicles have started the In Service Evaluation phase in Frankfurt with commercial flights. The First commercial flight that was dispatched with passengers from Frankfurt was flight LH130 on November 25, 2014.

Figure 53. TaxiBot NB releasing a B737 for flight after finalizing the taxiboting to Runway 18 in Frankfurt Airport

The 3 TaxiBot vehicles served in Frankfurt since November 2014 to dispatch the Lufthansa B737 fleet tile their last day of operation at October 31, 2016, when Lufthansa have closed the B737 fleet and transferred completely to A320 family for single aisle operation. The conclusion of the B737 operation in Frankfurt have shown, that the accumulated calculated fatigue damage recorder on hundreds of missions, is only about 60% of the authorized fatigues spectrum for TaxiBot operation. In addition, no incidents have been recorded during all two years of operation in Frankfurt.

Figure 54. TaxiBot NB, with A320neo during the certification test at Airbus Toulouse December 8, 2016

During November and December 2016, IAI have completed with Airbus the certification tests of the A320 family on the A320neo and A321neo instrumented airplanes at Airbus's Toulouse France facility. The formal EASA certificate is expected on March 2017 and will be followed by preparation trails with Lufthansa A320 fleet in order to make all the necessary preparations for the TaxiBot operation with the A321 and the A320neos of Lufthansa in Frankfurt.

The Wide Body TaxiBot for all the twin aisle airplanes (B747/767/777/787 and A330/340/350/380) is now in its operational testing period in Chateauroux France, using a simulated airplane testing trailer. The certification of the first WB airplane is expected next year, since the current low oil prices have slowed down its development process.

Figure 55. TaxiBot WB, with its testing trailer during maneuvering test

Summary of TaxiBot achievements and benefits:

- **TaxiBot is the Only Certified and Operational system for taxiing airplanes to takeoff with engines stopped**
- Reduction in Fuel consumption – 85%
- Emissions reduction CO2 & other noxious gasses – 85%
- Noise reduction – 60%
- FOD reduction – 50%
- Improve safety – No engine blast in gates area and better grip on contaminate taxiway
- Improve gates congestion & throughput – significant reduction of time wasted at cul-de-sacs (37%)
- Fast & Easy implementation:
- No modification to airplane systems – Achieved
- Pilot training by CBT no need for simulator – Approved & Working
- No extra weight & no impact on Cargo space – Achieved
- Minimal or no modifications to airports infrastructure – Achieved
- Minimal adaptations to existing procedures – Achieved
- Same concept for NB & WB airplanes

5 REFERENCES

1. Freed, Y., "Review of Aeronautical Fatigue Investigations in Israel, April 2013 – March 2015", *Minutes of the 34rd ICAF Conference*, Helsinki, Finland, 2015.

2. Buimovich Y. et al., A Summary of the G280 Executive Jet Full Scale Fatigue Test , 56th Israel Annual conference on Aerospace Sciences, 2016, Tel Aviv, Israel.

3. O. Heit et al., Determination of Safe Life Retirement Time of Helicopter Dynamic Components based on a Fretting Deterioration Model, Proceedings of the 56th Israel Annual Conference on Aerospace Sciences, 2016.

4. John H. Crews, Jr., Analytical and Experimental Investigation of Fatigue in a Sheet Specimen With an Interference-Fit Bolt, NASA Technical Note – TN D-7926, Langley Reseurcb Center, Humpton, Va. 23665, July 1975.

5. J. Y. Mann; A. S. Machin; W. F. Lupson and R. A. Pell, The Use of Interference-Fit Bolts or Bushes and Hole Cold Expansion for Increasing the Fatigue Life of Thick-Section Aluminum Alloy Bolted Joints, Department of Defense, Defense Science and Technology Organization, Aeronautical Research Laboratories, Mewourne. Victoria, Structures Note-409, August 1983.

6. J. M. Finney, Cold Expansion and Interference for Extending the Fatigue Life of Multi-Layer Metal, Joints, Department of Defense, Defense Science and Technology Organization, Aeronautical Research Laboratories, Mewourne. Victoria, Research Report 17, October 1993.

7. T. N .Chakherlou, M. Mirzajanzadeh, B. Abazadeh, K. Saeedi, An Investigation About Interference Fit Effect on Improving Fatigue Life of a Holed Single Plate in Joints, European Journal of Mechanics A/Solids, ELSEVIER, 29 (2010) pp. 675–682.

8. "StressCheck" FEM Computer Program, Version 10.1, June 2014, by ESRD.

9. "FATLAN" – FATigue Life ANalysis Computer Program, Version B.1.1 August 1992.

10. C. Matias and E. Katsav, Fatigue Evaluation For Hi-Lok Fastener Instalation Methods In Interference-Fit Holes, 56th Israel Annual conference on Aerospace Sciences, 2016, Tel Aviv, Israel.

11. Composite Material Handbook, Volume 3 – Polymer Matrix Composites Materials Usage, Design and Analysis

12. Mori, T. and Tanaka, K., Average stress in matrix and average elastic energy of materials with misfitting inclusions. Acta Metallurgica, 21, 571–574, 1973.

13. Aboudi J., The Generalized Method of Cells and High-Fidelity Generalized Method of Cells Micromechanical Models – A Review, Mechanics of Advanced Materials and Structures, 11, 2004.

14. Goose J.H. and Christensen S., Strain Invariant Failure Criteria for polymers in Composite Materials, AIAA-2001/1184, 2001.

15. Tay T.E. et al., Damage Progression by the Element-Failure Method (EFM) and the Strain Invariant Theory (SIFT), Composite Science and Technology, 65, 2005.

16. Tsai S.W. and Melo J.D.D, Composite Materials Design and Testing – Unlocking Mystery with Invariants, 2015.

17. Tsai S.W. and Melo J.D.D, An invariant based theory of composites, Composites Science and Technology 100, 237-243, 2014.

18. Freed Y., Implementation of Invariant-Based Approaches for Determination of Composite Materials Allowables, 56th Israel Annual conference on Aerospace Sciences, 2016, Tel Aviv, Israel.

19. Whitehead R.S., Kan H.P., Cordero R. and Saether E.S., Certification testing methodology for composite structures, Report No. NADC-87042-60, Volume I and II, 1986.

20. Tomblin J. and Seneviratne W., Determining the fatigue life of composite aircraft structures using life and load enhancement factors, FAA Report No. DOT/FAA/AR-10/6, 2011.

21. Ruiz Barragan J.M. et al, EADS CASA load enhancement factor to be applied on fatigue test for certification of composites, Proceedings of the 21st ICAF symposium, 2001.

22. Ratier L., How to test hybrid aircraft in fatigue, Proceedings of the 27th ICAF symposium, 2013.

23. Pfaller R., Gergely P. and Weinert A., Investigation on scatter of composites in comparison with metallic materials, Deutscher Luft- und Raumfahrkongress, Doc. ID 281342, 2012.

24. Giancaspro J., Taam W. and Wong R., Modified joint weibull approach to determine load enhancement factors, International Journal of Fatigue 31, 782-790, 2009.

25. Rouchon J. Fatigue and damage tolerance evaluation of structures – the composite materials response, 22nd Plantema Memorial Lecture, Proceedings of the 25th ICAF symposium, 2009

26. Rouchon J., How, over the past 20 years, part 25 composite structures have been coping with metal minded fatigue and damage tolerance requirements, Proceedings of the 24th ICAF symposium, 2007.

27. Elmalich D. and Freed Y., On the scatter factor in fatigue testing of composite material structures, 56th Israel Annual conference on Aerospace Sciences, 2016, Tel Aviv, Israel.

28. A. Brot, Developing Strategies to Combat Threats against the Structural Integrity of Aircraft, Proceedings of the 52nd Israel Annual Conference on Aerospace Sciences, 2012.

29. P. Safarian, Widespread Fatigue Damage Evaluation Method, Proceedings of the 27th ICAF Symposium, Jerusalem, 2013.

30. A. Brot, Optimizing the Inspection Intervals for Aircraft Structures Prone to Multi-Site Damage, Proceedings of the 53rd Israel Annual Conference on Aerospace Sciences, 2013.

31. D. Elmalich, A. Brot, Y. Freed, et al, A Risk Analysis Based Methodology for Widespread Fatigue Damage Assessment, Proceedings of the 55th Israel Annual Conference on Aerospace Sciences, 2015.

32. Y. Freed, D. Elmalich, A. Brot, et al, A Risk Analysis Based Methodology for Widespread Fatigue Damage Evaluation, Proceedings of the 28th ICAF Symposium, Helsinki, 2015.

33. A. Brot, Optimization Strategies for Minimizing Fatigue Failures in Metallic Structures, Presented to the 31st Israel Conference on Mechanical Engineering, 2010.

34. J. Gallagher, A Review of the Philosophies, Processes, Methods and Approaches that Protect In-Service Aircraft from the Scourge of Fatigue Failures, Plantema Memorial Lecture, Proceedings of the 24th ICAF Symposium, Naples, 2007.

35. A. Brot, Selection of an Acceptable Risk Criterion for Avoiding a Major Fatigue Failure on a Commercial Aircraft, 56th Israel Annual conference on Aerospace Sciences, 2016, Tel Aviv, Israel.

36. NASGRO - Fracture Mechanics and Fatigue Crack Growth Analysis Software; Version 8.1; May, 2016 Manual.

37. J. Tweed, and D.P. Rooke, “The Elastic Problem for an Infinite Solid Containing a Circular Hole with a Pair of Radial Edge Cracks of Different Lengths,” International Journal of Engineering Science, Vol. 14, No. 10, pp. 925-933.

38. Y. Bombardier, G. Renaud, and M. Liao, “Stress Intensity factor Solutions for Cracks at a Hole in an Infinite Sheet,” National Research Council Canada, LTR-SMPL-2010-0117, Ottawa.

39. M.P. Weiss The use of classification zones for fatigue behavior in steels. ASME J Eng Mater Technol 1977(1):22–5.

40. M.P.Weiss, "Estimating fatigue cracks, from the onset of loading, in AISI 4340 specimens, under cyclic stresses," Int. J. Fatigue, vol. 2, no. 14 , pp. 91-96, 1992.

41. M.P. Weiss and E. Lavie, “Fatigue of Metals – What the designer needs? International Journal of Fatigue 84 (2016) 80–90.

42. M. Perl et al., 3-D Stress Intensity Factors due to Autofrettage for an Inner Radial Lunular or Crescentic Crack in a Spherical Pressure Vessel, Engineering Fracture Mechanics, 131,p. 282-295, 2014.

43. Q. Ma et al., The Bauschinger Effect’s Influence on the SIFs of a Semi-Elliptical Crack Emanating from an Erosion at the Bore of a Fully Autofrettaged Pressurized Cylinder, Journal of Pressure Vessel Technology, 137, 2015.

44. M. Perl and M. Steiner, 3-D Stress Intensity Factors due to Full Autofrettage for Inner Radial or Coplanar Crack Arrays and Ring Cracks in a Spherical Pressure Vessel, Engineering Fracture Mechanics, 138, p. 233-249, 2015.

45. Q. Ma et al., The Effects of Crack Ellipticity on the Mode I SIFs of a Simulated Eroded Pressurized Cylinder, Procedia Engineering, 130, p. 711-730, 2015.

46. Q. Ma et al., 3-D Interaction of a Corner Flaw with a Non-Aligned Surface Flaw in an Infinitely Large Plate under Tension, Procedia Engineering, 130, p. 1288-1297, 2015.

47. M. Perl and M. Steiner, The Beneficial Effect of Full or Partial Autofrettage on the Combined 3-D Stress Intensity Factor for an Inner Radial Lunular or Crescentic Crack in a Spherical Pressure Vessel, Engineering Fracture Mechanics, 156, p. 124-140, 2016.

48. M. Perl and M. Steiner, 3-D Stress Intensity Factors due to Full Autofrettage for Inner Radial or Coplanar Crack Arrays and Ring Cracks in a Spherical Pressure Vessel, Procedia Structural Integrity, 2, p. 3625-3646, 2016.

49. M. Perl et al., The influence of a non-aligned semi-elliptical surface crack on a quarter-circle corner crack in an infinitely large plate under uniaxial tension, AIMS Materials Science, 3, p. 1474-1492, 2016.

50. Kawai M, Koizumi M. Nonlinear constant fatigue life diagrams for carbon/epoxy laminates at room temperature. Compos: Part A 2007; 38(11):2342–53.

51. Kawai M, Teranuma T. a multiaxial fatigue criterion based on the principal constant life diagrams for unidirectional carbon/epoxy laminates. Compos: Part A 2012; 43(2012):1252-1266.

52. B. Harris, A parametric constant-life model for prediction of the fatigue lives of fibre-reinforced plastics, in fatigue in composites, ed. by B. Harris (Woodhead Publishing Limited, Cambridge, UK, 2003), pp. 546-568.

53. I. Greenfeld and D. Wagner, Nanocomposite toughness, strength and stiffness: role of filler geometry, Nanocomposites, 1, p. 3-17, 2015.

54. X. Sui et al., Multilevel composite using carbon nanotube fibers (CNTF), Composite Science and Technology, 137, p. 35-43, 2016.

55. L. Yang et al., Toughness of carbon nanotubes conforms to classic fracture mechanics, Science Advances, 2, doi: 10.1126/sciadv.1500969, 2016.

56. K. Livanov et al., Tough Alumina/Polymer Layered Composites with High Ceramic Content, J. Am. Ceram. Soc., 98, p. 1285–1291, 2015.

57. K. Livanov et al., Interphase tuning for stronger and tougher composites, Scientific Reports 6, doi:10.1038/srep26305, 2016.

58. S. Konforty et al., Bearing health monitoring using optical fiber sensors, 3rd European Conference of the Prognostics and Health Management Society, 2016.

59. D. Shalev et al., Condition Based Reliability, Availability, Maintainability, and Safety (CB-RAMS) model: Improving RAMS predictions by combining condition-monitoring (CM) data with RAMS calculations, 3rd European Conference of the Prognostics and Health Management Society, 2016.

60. R. Peretz et al., Detection of Fatigue Cracks in Shafts via Analysis of Vibrations and Orbital Paths, Annual Conference of the Prognostics and Health Management Society, 2016.

61. N. Koren, Steps toward fault prognostics of gears, The 13th International Conference on Condition Monitoring and Machinery Failure Prevention Technologies, Paris, France, 2016.

62. A. Brot, Three faces of aeronautical fatigue, 29th symposium on the international committee on aeronautical fatigue and structural integrity (ICAF), Plantema lecture, Nagoya, Japan, 2017.

63. Mittelman Brigit and Yosibash Z. ,``Energy release rate cannot predict crack initiation orientation in domains with a sharp V-notch under mode III loading", *Engineering Fracture Mechanics,* 141, pp. 230-241, (2015).

64. Yosibash Z. and Mittelman B., "A 3D Failure Initiation Criterion from a Sharp V-notch Edge in Elastic Brittle Structures", European Journal of Mechanics - A/Solids, 60, pp. 70-94, (2016).

65. Shannon, S., Peron, V. and Yosibash Z, ``The Laplace equation in 3-D domains with cracks: Dual singularities with log terms and extraction of corresponding edge flux intensity functions", *Mathematical Methods in the Applied Sciences*, **34**, pp. 4951–4963 (2016).

66. Yosibash Z. and Mittelman B., "A Revised Failure Criterion for Brittle Elastic Materials Under Mixed-mode Loading in 2-D", Theoretical and Applied Fracture Mechanics, 84, pp. 149–156, (2016).

67. T. Simhi, L. Banks-Sills, V. Fourman and A. Shlayer, ”Mode I Fracture Toughness of CNT Reinforced PMMA”, Strain, 51 (2015) 474–482

68. L. Banks-Sills, T. Simhi and V. Fourman, ”Fracture Toughness Measurements of PMMA Reinforced with CNTs”, ESIS Technical Committee 4, Les Diablerets, Switzerland (2015).

69. D.G. Shiber, “Mechanical Properties of Poly (Methyl Methacrylate) Enhanced by Functionalized Carbon Nano Tubes”, M.Sc., Tel Aviv University (2015).

70. L. Banks-Sills, D.G. Shiber, V. Fourman, R. Eliasi and A. Shlayer, ”Experimental Determination of Mechanical Properties of PMMA Reinforced with Functionalized CNTs”, Composites Part B, 95 (2016) 335–345

71. L. Banks-Sills, ”Interface Fracture Mechanics - Theory and Experiment”, International Journal of Fracture 191 (2015) 131–146.

72. L. Banks-Sills, ”Statistical Analysis for Interface Fracture and Delamination Failure of Composites”, The Josef Singer Memorial Lecture (invited), Technion, Haifa, Israel (2015).

73. L. Banks-Sills. Delamination Failure of Composites Statistical Analysis, Italian Group of Fracture (invited), Favignana, Italy (2015).

74. L. Banks-Sills, “Statistical Analysis of Delamination Failure of Composites” (plenary), Advanced Problems in Mechanics, St. Petersburg, Russia (2016).

75. L. Banks-Sills, Y. Freed, R. Eliasi and V. Fourman, “Fracture Toughness of the +45◦/–45◦ Interface of a Laminate Composite”, International Journal of Fracture, 141 (2006) 195–210.

76. Ido Simon, “Delamination Propagation in a DCB Specimen Composed of a Plain Weave Multi-Directional Laminate Composite Subjected to Different Cyclic Displacement Ratios”, M.Sc., Tel Aviv University (2016).

77. I. Simon, L. Banks-Sills, V. Fourman and R. Eliasi, “Fatigue Delamination Propagation in a DCB Specimen Composed of a Plain Weave Multi-Directional Laminate Composite Subjected to Different Load Ratios”, 56th Israel Annual Conference on Aviation and Astronautics, Israel (2016).

78. I. Simon, L. Banks-Sills, V. Fourman and R. Eliasi, “Delamination Propagation and Load Ratio Effects in DCB MDWoven Composite Specimens”, European Conference of Fracture (ECF21), Procedia Structural Integrity, Catania, Italy (2016).

79. L. Banks-Sills, I. Simon and V. Fourman, “Fatigue Delamination Propagation in DCB MD Woven Composite Specimens”, International Conference of Experimental Mechanics (ICEM17), Rhodes, Greece (2016).

80. I. Simon, L. Banks-Sills and V. Fourman, ”Mode I Delamination Propagation and R-Ratio Effects in Woven Composite DCB Specimens for a Multi-Directional Layup”, International Journal of Fatigue, 96 (2017) 237-251.

81. E. Farkash, “Reappraisal the Virtual Crack Closure Technique for Accurately Calculating Stress Intensity Factors for Interface Cracks”, M.Sc., Tel Aviv University (2016).

82. L. Banks-Sills and E. Farkash, ”A Note on the Virtual Crack Closure Technique for an Interface Crack”, International Journal of Fracture, 201 (2016) 171–180.

83. L. Banks-Sills and E. Farkash, “Reassessment of the Virtual Crack Closure Technique for Interface Cracks”, International Congress of Applied and Theoretical Mechanics (ICTAM24), Montreal, Canada (2016).

84. I. Simon, L. Banks-Sills and V. Fourman, “Mode I Fatigue Delamination Propagation in Unidirectionally Reinforced Materials TC4 Round Robin”, ESIS Technical Committee 4, Les Diablerets, Switzerland (2016).

85. Haj-Ali, R., and Aboudi, J.,” Integrated Microplane Model with the HFGMC Micromechanics for Nonlinear Analysis of Composite Materials with Evolving Damage” Int. J. Solids and Structures, Vol 90, pp. 129–143, 2016.

86. Levi-Sasson, A., Aboudi, J., Matzenmiller, A., and Haj-Ali, R. Failure Envelopes for Laminated Composites by the Parametric HFGMC Micromechanical Framework. Composite Structures. Vol. 140:15,pp. 378–389, 2016.

87. A. Baker, F. Rose, R. Jones (Editors), Advances in the bonded composite repair of metallic aircraft structure, Elsevier, 2002.

88. R. Jones, S. Galea, 2002. "Health monitoring of composite repairs and joints using optical fibers", Composite Structures, 58:397–403.

89. J. Leng, and A. Asundi, 2003. "Structural health monitoring of smart composite materials by using EFPI and FBG sensors", Sensors and Actuators A: Physical, 103(3):330-340.

90. M. Mulle, F. Collombet, P. Olivier, Y.-H. Grunevald, “Assessment of cure residual strains through the thickness of carbon–epoxy laminates using FBGs”, Part I: Elementary specimen, Composites: Part A 40, 94–104 (2009)

91. E. Chehura, A. A. Skordos, C-C Ye, S. W. James, I. K. Partridge, R. P. Tatam, “Strain development in curing epoxy resin and glass fibre/epoxy composites monitored by fibre Bragg grating sensors in birefringent optical fibre”, Smart Mater. Struct. 14, 354–362 (2005)

92. Andreas, O., and Kyriacos, K., Fiber Bragg Grating. Fundamentals and Applications in Telecommunications and Sensing. Artech House, 1999.

93. C. D. Butter, G. B. Hocker, “Fiber optics strain gauge,” Appl. Opt. 17, 2867-2869 (1978).

94. 14CFR Part 25 “Airworthiness Standards: Transport Category Airplanes”.